Publications of the Astronomical Society of Japan, 2024, **00**, 1–19
doi: 10.1093/pasj/xxx000
Advance access publication date:

The Galactic-Centre Arms inferred from ALMA CMZ Exploration Survey - ACES -

Yoshiaki SOFUE[1], Tomoharu OKA[2], Steven N. LONGMORE[3,4], Daniel WALKER[5], Adam GINSBURG[6], Jonathan D. HENSHAW[3,7], John BALLY[8], Ashley T. BARNES[9], Cara BATTERSBY[10], Laura COLZI[11], Paul HO[12], Izaskun JIMENEZ-SERRA[11], J. M. Diederik KRUIJSSEN[13,4], Elizabeth MILLS[14], Maya A. PETKOVA[15], Mattia C. SORMANI[16,17], Jen WALLACE[10], Jairo ARMIJOS-ABENDAÑO[18], Katarzyna M. DUTKOWSKA[19], Rei ENOKIYA[20], Yasuo FUKUI[21], Pablo GARCÍA[22,23], Andres GUZMAN[24], Christian HENKEL[25], Pei-Ying HSIEH[26], Yue HU[27], Katharina IMMER[9], Desmond JEFF[6,28], Ralf S. KLESSEN[29,30,31,32], Kotaro KOHNO[1], Mark R. KRUMHOLZ[33], Dani LIPMAN[10], Mark R. MORRIS[34], Francisco NOGUERAS-LARA[9], M. NONHEBEL[9,35], Jürgen OTT[36], Jaime E. PINEDA[37], Sergio MARTÍN[38,39], Miguel Angel REQUENA-TORRES[40], Víctor M. RIVILLA[11], Denise RIQUELME-VÁSQUEZ[41], Álvaro Sánchez-Monge[42,43], Howard A. SMITH[32], Tabassum S TANVIR[44], Volker TOLLS[31], and Q. Daniel WANG[45]

[1]Institute of Astronomy, The University of Tokyo, Mitaka, Tokyo 181-0015, Japan
[2]Department of Physics, Faculty of Science and Technology, Keio University, 3-14-1 Hiyoshi, Yokohama, Kanagawa 223-8522, Japan
[3]Astrophysics Research Institute, Liverpool John Moores University, IC2, Liverpool Science Park, 146 Brownlow Hill, Liverpool L3 5RF, UK
[4]Cosmic Origins Of Life (COOL) Research DAO, https://coolresearch.io
[5]UK ALMA Regional Centre Node, Jodrell Bank Centre for Astrophysics, Oxford Road, The University of Manchester, Manchester M13 9PL, United Kingdom
[6]Department of Astronomy, University of Florida, P.O. Box 112055, Gainesville, FL 32611
[7]Max Planck Institute for Astronomy, Königstuhl 17, D-69117 Heidelberg, Germany
[8]Center for Astrophysics and Space Astronomy; Department of Astrophysical and Planetary Sciences; University of Colorado, Boulder, CO 80389, USA
[9]European Southern Observatory (ESO), Karl-Schwarzschild-Strasse 2, 85748 Garching, Germany
[10]Department of Physics, University of Connecticut, 196A Auditorium Road, Unit 3046, Storrs, CT 06269, USA
[11]Centro de Astrobiología (CAB), CSIC-INTA, Carretera de Ajalvir km 4, Torrejón de Ardoz, 28850 Madrid, Spain
[12]AS/NTU Astronomy-Mathematics Building, Roosevelt Rd, Taipei 10617, Taiwan
[13]Technical University of Munich, School of Engineering and Design, Department of Aerospace and Geodesy, Arcisstr. 21, 80333 Munich, Germany
[14] Department of Physics and Astronomy, University of Kansas, 1251 Wescoe Hall Drive, Lawrence, KS 66045, USA
[15]Space, Earth and Environment Department, Chalmers University of Technology, SE-412 96 Gothenburg, Sweden
[16]Università dell'Insubria, via Valleggio 11, 22100 Como, Italy
[17]Department of Physics, University of Surrey, Guildford GU2 7XH, UK
[18]Observatorio Astronómico de Quito, Observatorio Nacional, Escuela Politécnica Nacional, Interior del Parque La Alameda, 170136, Quito, Ecuador
[19]Leiden Observatory, Leiden University, P.O. Box 9513, 2300 RA Leiden, The Netherlands
[20]Kyuushu Sangyo University, Fukuoka, Japan
[21]Department of Physics, Nagoya University, Chikusa-ku, Nagoya 464-8602, Japan
[22]Chinese Academy of Sciences South America Center for Astronomy, National Astronomical Observatories, CAS, Beijing 100101, China
[23]Instituto de Astronomía, Universidad Católica del Norte, Av. Angamos 0610, Antofagasta, Chile
[24]Joint ALMA Observatory, Alonso de Cordova 3107, Vitacura 763-0355, Santiago de Chile, Chile
[25]MPIfR, Auf dem Hügel 69, Bonn, Germany
[26]National Astronomical Observatory of Japan, 2-21-1 Osawa, Mitaka, Tokyo 181-8588, Japan
[27]Institute for Advanced Study, 1 Einstein Drive, Princeton, NJ 08540, USA
[28]National Radio Astronomy Observatory, 520 Edgemont Road, Charlottesville, VA 22903, USA
[29]Universität Heidelberg, Zentrum für Astronomie, Institut für Theoretische Astrophysik, Albert-Ueberle-Str. 2, 69120 Heidelberg, Germany
[30]Universität Heidelberg, Interdisziplinäres Zentrum für Wissenschaftliches Rechnen, Im Neuenheimer Feld 225, 69120

Received: , **Accepted:**

Heidelberg, Germany
[31]Center for Astrophysics | Harvard & Smithsonian, 60 Garden Street, Cambridge, MA, 02138, USA
[32]Elizabeth S. and Richard M. Cashin Fellow at the Radcliffe Institute for Advanced Studies at Harvard University, 10 Garden Street, Cambridge, MA 02138, USA
[33]Research School of Astronomy and Astrophysics, Australian National University, Cotter Road, Weston ACT 2611, Australia
[34]Department of Physics and Astronomy, University of California, Los Angeles, CA 90095, USA
[35]SUPA,School of Physics and Astronomy, University of St. Andrews, North Haugh, St. Andrews KY16 9SS, UK
[36]National Radio Astronomy Observatory, P.O. Box O, 1011 Lopezville Road, Socorro, NM 87801, USA
[37]MPI for Extraterrestrial Physics, Giessenbachstr. 1, D-85748, Garching by Muenchen, Germany
[38]European Southern Observatory, Alonso de Córdova, 3107, Vitacura, Santiago 763-0355, Chile
[39]Joint ALMA Observatory, Alonso de Córdova, 3107, Vitacura, Santiago 763-0355, Chile
[40]Department of Physics, Astronomy, and Geosciences, Towson University, Towson, MD 21252, USA
[41]Departamento de Astronomía, Universidad de La Serena, Raúl Bitrán 1305, La Serena, Chile
[42]Institut de Ciències de l'Espai (ICE), CSIC, Campus UAB, Carrer de Can Magrans s/n, E-08193, Bellaterra (Barcelona), Spain
[43]Institut d'Estudis Espacials de Catalunya (IEEC), E-08860, Castelldefels (Barcelona), Spain
[44]Department of Physics and Astronomy, Iowa State University, 2323 Osborn Drive, Ames, IA 50010, USA
[45]Department of Astronomy, University of Massachusetts, Amherst, MA 01003, USA

*E-mail: sofue@ioa.s.u-tokyo.ac.jp

ORCID: 0000-0002-4268-6499, 0000-0002-5566-0634, 0000-0001-6353-0170, 0000-0001-7330-8856, 0000-0001-6431-9633, 0000-0001-9656-7682, 0000-0001-8135-6612, 0000-0003-0410-4504, 0000-0002-6073-9320, 0000-0001-8064-6394, 0000-0002-3412-4306, 0000-0003-4493-8714, 0000-0002-8804-0212, 0000-0001-8782-1992, 0000-0002-6362-8159, 0000-0001-6113-6241, 0000-0000-0000-0000, 0000-0003-3341-6144, 0000-0003-0980-6871, 0000-0001-0000-0000, 0000-0002-8966-9856, 0000-0002-7495-4005, 0000-0001-9155-3978, 0000-0002-8455-0805, 0000-0003-4140-5138, 0000-0003-0416-4830, 0000-0002-0560-3172, 0000-0002-4052-2394, 0000-0003-3893-854X, 0000-0002-5776-9473, 0000-0002-6753-2066, 0000-0002-6379-7593, 0000-0000-0000-0000, 0000-0001-8224-1956, 0000-0002-3972-1978, 0000-0001-9281-2919, 0009-0009-5346-7329, 0000-0002-2887-5859, 0000-0001-5389-0535, 0000-0002-3078-9482, 0000-0002-0862-0701, 0000-0003-1841-2241, 0000-0002-9279-4041

Abstract

Based on the analysis of longitude-velocity diagrams (LVDs) in the CS ($J=2-1$) and H^{13}CN ($J=1-0$) molecular lines from the ACES (ALMA CMZ Exploration Survey) internal release data and ^{13}CO ($J=1-0$) from Nobeyama 45-m Galactic-Centre survey, we identify six Galactic-Centre (GC) arms as straight LV ridges extending over ±100 km s^{-1}. In addition to the currently known Arms I to IV,we identify a new inner arm which we call Arm V, and further highlight the circum-nuclear disc (CND) as Arm VI. By applying the LV-ridge masking method, we obtain moment 0 or integrated intensity maps of the Arms on the sky, which suggest that most of the Arms compose ring-like structures inclined from the Galactic plane. We further determine the radii (curvatures) of the Arms using the velocity-gradient (dv/dl) method, assuming that the arms are rotating on circular orbits at a constant velocity of ~100–150 km s^{-1}(flat rotation curve). We thus show that Arms I and II compose the main ring-like structure of the CMZ with radii ~100–120 pc; Arm III is 42 pc from the GC and is associated with the 20-km s^{-1}cloud; Arm IV is an arm 20 pc from the GC, which is clear and narrow in the LVD; and Arm V is a faint, long arm at 9 pc radius that has a ring nature tilted from the Galactic plane and is associated with the 50-km s^{-1}cloud. We show that the circumnuclear disc (CND), here we identify it as Arm VI, is an inclined molecular ring of radius ~2 pc associated with bifurcated spiral fins. These radii fall on an empirical relation $R\sim630(2/5)^N$ for $N=1$ (Arm I) to 6 (VI), suggesting either discrete orbital rings or a logarithmic spiral with pitch angle $\sim22^\circ$. The vertical thickness of the arm increases with radius and is approximately represented by $z\sim0.7(R/1\ \mathrm{pc})^{0.7}$ pc, and the tilt angle of the arms from the Galactic plane, or the warping, increases rapidly toward the GC.

Keywords: Galaxy : centre — Galaxy : structure — ISM : clouds — ISM : molecules — ISM : kinematics and dynamics

1 Introduction

Because we see the Galactic Central Molecular Zone (CMZ) edge-on, its true 3D structure is challenging to decipher and remains substantially uncertain (Morris & Serabyn 1996; Henshaw et al. 2016; Sofue 2022; Henshaw et al. 2023). Kinematic analysis of longitude-velocity diagrams (LVDs), assuming Galactic rotation, offers one way to help to resolve line-of-sight degeneracy (Bally et al. 1987; Bally et al. 1988; Sofue 1995; Sofue 2022; Oka et al. 1998; Tsuboi et al. 1999; Kruijssen et al. 2015 ; Henshaw et al. 2016; Henshaw et al. 2023). Here, we exploit the special behavior of a rotating arm or a ring in the longitude-velocity diagram (LVD), which makes the LV ridge to appear sharpest near its intersection with the rotation axis at $l\sim0^\circ$. The absorption of line emission against the background continuum helps to distinguish the far and near sides of clouds relative to Sgr A* (Sawada et al. 2004 ; Yan et al. 2017; Sofue 2022).

Coherent ridges on the LVD suggest that the CMZ is structured into multiple arms. The densest and most prominent LV ridge seen in the ^{13}CO ($J=1-0$) line is called Galactic-Centre (GC) Arm I, the second is Arm II, and further arms (III and IV) have been proposed (Sofue 1995). There seems to be consensus that Arms I and II compose a ring structure of radius $\sim$ 100-120 pc (the "120-pc ring") (Sofue 1995; Oka et al. 1998; Tokuyama et al. 2019; Henshaw et al. 2016; Henshaw et al. 2023), which is understood as due to a large-scale accretion of gas from the outer Galactic disc (Molinari et al. 2011; Kim & Stone 2012; Kruijssen et al. 2015 ; Krumholz & Kruijssen 2015; Krumholz et al. 2017; Ridley et al. 2017; Sormani et al. 2019 ; Sormani et al. 2020; Tress et al. 2020).

However, the more internal structure of molecular gas within the CMZ inside 120 pc ring appears to have not yet been fully explored, but is believed to consist of a continuous disc, arm/rings or a hole (empty space), or a combination of these. Among these the arm/ring structure can be most easily recognized using high-resolution molecular-line mapping data, while the other structures may be obtained as the residual. For the purpose to map arms/rings of molecular gas, we analyze the data cubes observed with the Nobeyama 45-m telescope in the ^{13}CO ($J=1-0$)line, ASTE (Atacama Submm Telescope Experiments) 10-m telescope in HCN ($J=4-3$), and ALMA (Atacama Large Millimeter/submillimeter Array) in the course of the large project ACES (ALMA CMZ Exploration Survey) in CS ($J=2-1$) and H^{13}CN ($J=1-0$) lines (ALMA Program, 2021.1.00172.L. PI: S. Longmore et al. in preparation). Thanks to the high spatial resolu-

tion offered by ALMA, we can much improve arm-identification at the very center inside $|l| \lesssim 0^\circ.2 (\sim 30\ \mathrm{pc})$.

The region around Sgr A* contains many well-known molecular clouds, including the 50-km s^{-1} cloud (hereafter 50kmC) (Tsuboi et al. 2009), 20-km s^{-1} cloud (20kmC) (Takekawa et al. 2017a), high-velocity compact clouds (HVCCs) (Oka et al. 1999; Iwata et al. 2023), the circum-nuclear disk (CND) (Wright et al. 2001; Tsuboi et al. 2018), and the mini-spirals around Sgr A* (Tsuboi et al. 2017). We try to understand these innermost structures under a unified view of a molecular disc with arms/rings rapidly rotating in the deep gravitational potential which reaches the specific kinetic energies of $\sim V_{\rm rot}^2/2 \sim 10^{14}$ erg g^{-1} at $V_{\rm rot} \sim 100$–150 km s^{-1}.

In this study, we combine ^{13}CO ($J=1-0$) and HCN ($J=4-3$) single-dish data with the ACES interferometric mosaics in the CS ($J=2-1$)and H^{13}CN ($J=1-0$) at $|l| \lesssim 0^\circ.2$ to determine the internal kinematical structure of the CMZ by constraining the radii and vertical extents of the arms/rings present within ~ 100 pc. This will help us to visualize the gaseous structure in the circum-nuclear region, which is essential to carry out the 3D modeling of the CMZ.

We adopt a Solar galactocentric distance $R_0 = 8.2$ kpc, close to the recent measurement (Gravity Collaboration et al. 2019), for convenience to compare with the other works. The coordinates of Sgr A* is taken to be $(l, b) = (359^\circ.944227, -0^\circ.046157) = (359^\circ 56' 39''.2, -00^\circ 02' 46''.2)$, and the LSR (Local Standard of Rest) velocity is assumed to be $v_{\rm LSR} = 0$ km s^{-1}.

2 Data and analysis

2.1 Single-dish data

We used the archival data cube of the ^{13}CO ($J=1-0$) line emission at 110.27 GHz taken from the CMZ survey obtained using the Nobeyama 45-m telescope (Tokuyama et al. 2019). The data cube had a sampling grids of ($7''.5 \times 7''.5 \times 2$ km s^{-1}) with an effective resolution of $16.7''$ which yields rms noise of ~ 0.15 K in brightness temperature, $T_{\rm B}$. We also used an archival data cube of the HCN ($J=4-3$) line emission at 354.5 GHz from the GC survey with the ASTE 10-m telescope (Tanaka et al. 2018), which had ($8''.5 \times 8''.5 \times 2$ km s^{-1}) grids with an effective angular resolution of $24''$ and rms noise of 0.14 K in $T_{\rm B}$.

2.2 ACES

The molecular-line cubes from ALMA used in this work were taken from the internal release version of the 12m+7m+TP (Total Power)-mode data from the ALMA cycle 8 Large Program "ALMA Central Molecular Zone Exploration Survey" (ACES, 2021.1.00172.L; Longmore et al. in preparation). ACES observed the CMZ in ALMA Band 3, covering a frequency range of $\sim$ 86 - 101 GHz across six spectral windows of varying spectral resolution and bandwidth.

The ALMA pipeline calibrated measurement sets were produced using CASA 6.4.1.12, and all of the 12m and 7m data were re-imaged using CASA 6.4.3-2. In general the imaging parameters were the same as those used by the pipeline to produce the delivered data, but there were instances where parameters were changed, in particular to fix divergent channels, and to undo size mitigation performed by the default pipeline parameters.

We also found that the ALMA pipeline often did not perform optimally when identifying the line-free channels in the data, resulting in residual continuum emission after performing the continuum subtraction. The pipeline also used a polynomial fit order of 1, which often resulted in poor baselines after continuum subtraction, particularly in the narrow spectral windows which are often filled with broad line emission. To fix these issues, we first re-ran the continuum subtraction using a fit order of 0, and then additionally used `statcont` (Sánchez-Monge et al. 2018) to remove the residual continuum emission. After re-imaging and subtracting the continuum, we combined the 12m, 7m, and TP data using the `feather` task in CASA. We first combined the 7m and TP cubes, then combine this 7m+TP cube with the 12m data.

The ACES coverage is split into 45 individual sub-mosaics, each with approximately 150 pointings. For each line/SPW, we used the `radio-beam` and `reproject` Python packages to convolve all sub-mosaics to a common beam, and then project on to the full ACES footprint. The resulting cubes provide a contiguous mosaic of the CMZ.

For this work, we used the cubes in the CS ($J=2-1$) line at a frequency 97.9810 GHz with FWHM angular resolution $2''.21$ of the synthesized beam and rms noise of 0.0038 Jy beam^{-1} (0.10 K) with velocity channel increment of 1.45 km s^{-1}, and H^{13}CN ($J=1-0$) line at 86.3399 GHz with resolution $2''.72$ and rms noise 0.0046 Jy beam^{-1} (0.10 K) with a velocity channel increment 0.88 km s^{-1}. The intensity scales are Jy beam^{-1} (1 Jy beam^{-1}= 26.1 and 22.2 K in brightness temperature at 98 and 86 GHz, respectively).

The cubes cover the CMZ at $-0^\circ.6 \lesssim l \lesssim +0^\circ.9$ and $-0^\circ.3 \lesssim b \lesssim +0^\circ.1$, and velocity ranges were $-220 \leq v_{\rm LSR} \leq +220$ km s^{-1} and $-150 \leq v_{\rm LSR} \leq +150$ km s^{-1}, respectively, with spatial and velocity grids of ($0''.5 \times 0''.5 \times 0.15$ km s^{-1}). We further cut out a more interior region at $-0^\circ.25 \leq l \leq +0^\circ.15$ and $-0^\circ.1 \leq b \leq +0^\circ$ for a detailed analysis of the circum-nuclear region centered on Sgr A*.

2.3 Definition and identification of the Arms

The goal of this paper is to identify spiral arms, rings, and/or segments thereof (hereafter "arms") in the CMZ that rotate within the Galactic gravitational potential, and to quantify their galactocentral radii or curvatures. An "arm" is here defined by a tilted ridge on the LVD that extends straightly for $\sim \pm 100$ km s^{-1}, indicating a coherent ring-like structure rotating at $\sim$ 100–150 km s^{-1}.

We used the ^{13}CO ($J=1-0$) line from the single dish in order to trace the arms and extended structure in the entire CMZ. The lines CS ($J=2-1$) and H^{13}CN ($J=1-0$) from the ALMA cubes were chosen to trace the innermost arms, which are supposed to consist of relatively denser molecular gas (Shirley 2015), for a complementary analysis to the ^{13}CO ($J=1-0$) line from the single dish.

To identify the arms, we exploit a special property of the LVD that, due to the degeneracy of the radial velocity, arms appear clearest and brightest near their intersection with the axis of rotation at $l \sim 0^\circ$. Although some arms overlap at $l \sim 0^\circ$, they can be distinguished from one another because their ridges run at different tilt angles (Sofue 2006). Fortunately, non-circular motions of the arms overlap, so in most cases the degeneracy is resolved by the displacement of the radial velocity from zero at the intersection point. Note that there are four ways to display LVD: channel LVD (at every latitude as one channel of the cube), total average (moment 0 over all latitudes), average for selected latitudes, and maximum intensity (peak $T_{\rm B}$ across latitudes). They are all used in this work depending on the purpose of each figure.

Nevertheless, especially in the central region, the LV arms are often buried in bright extended features. In order to abstract such buried arms by subtracting more extended structures, we apply the IMSHIFT relieving technique described in Appendix 1. This method is particularly useful for the single-dish data with lower angular resolution.

By tracing the tilted LVD ridge (LVR), we measure the longitudinal velocity gradient dv/dl, which is related to the radius or the curvature of the arm as explained in detail in section 4.1. For identifying a spiral arm or a ring, this method is more sensitive and accurate than measuring the terminal velocity ends at the farthest longitudes, because the inherent width and velocity dispersion make it difficult to define the exact terminal longitude and velocity.

2.4 LVD "Arms"

We search for arms in all channels of the cubes as LV ridges with extents over +/- 100 km/s. In figures 1 to 6 we show the LVDs at representative latitudes of the thus recognized GC Arms in the ^{13}CO $(J=1-0)$ line from Nobeyama 45 m, HCN $(J=4-3)$ from ASTE 10 m, and CS $(J=2-1)$ and H^{13}CN $(J=1-0)$ from ALMA. Details of the data are shown in individual panels of the figures and captions. The identified arms are marked by the white dashed lines or arrows with corresponding names.

The arms are often too thin and faint to be recognized on a single or an averaged LVD. In order to convincingly trace such arms in more detail, we also use channel LVDs as presented in Appendix 2 (figures 21 to 24).

In figure 7 we summarize all the identified arms by dashed lines superposed on the maximum-intensity LVD from ALMA in the whole mapped area by ACES in CS $(J=2-1)$ from $b=-0.^{\circ}3$ to $+0.^{\circ}2$. The middle and bottom panels show the same in CS $(J=2-1)$ and H^{13}CN $(J=1-0)$, but for the central region from $l=-0.^{\circ}25$ to $0.^{\circ}15$, and $b=-0.^{\circ}1$ to 0°. These LVDs were made by creating maximum intensity projections along the latitude axis of the cubes using the `spectral-cube` Python package.

2.5 Vertical profiles of the Arms

Figure 8 shows latitudinal intensity profiles of the Arms at representative points on the LV ridges. Note that the latitude range is $0.^{\circ}6$ for Arms I to III, while it is $0.^{\circ}1$ for IV to VI. We measured the vertical thickness of the arms using latitudinal intensity profiles shown in figure 8, where the arm's full b width z was measured at $\sim 20\%$ level of intensity maximum.

The full width of the arms are thus obtained to be $z\sim 0.^{\circ}18\sim 26$ pc for Arm I, $\sim 0.^{\circ}14\sim 20$ pc for Arm II; $\sim 0.^{\circ}033\sim 4.7$ pc for Arm III; $\sim 0.^{\circ}025\sim 3.6$ pc for Arm IV; $\sim 0.^{\circ}022\sim 3.1$ pc for Arm V; and $\sim 0.^{\circ}010\sim 1.4$ pc for Arm VI (CND). We emphasize that the vertical width of the arms decreases significantly from Arm I to VI, which will be discussed in section 4.1. The derived quantities are listed in table 1.

2.6 Arms on the sky (moment 0 maps along LV ridges): The LV-masking method

We then produce integrated intensity (moment 0) maps around the LV ridges of Arm I to VI (CND) indicated by the dashed lines in the LVDs in figures 1 through 7. We produce these maps by using a "masked cube" created by convolving the original cube with a cube of the same size (masking cube) representing a Gaussian function,

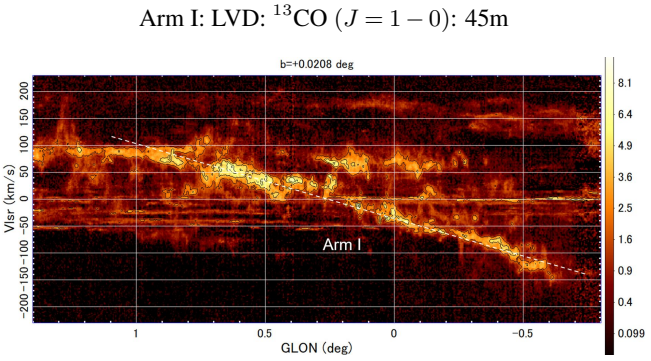

Fig. 1. Longitude-velocity diagram (LVD) showing the Galactic-Centre (GC) Arm I in ^{13}CO $(J=1-0)$ line by 45m at a representative latitude. Color bars indicate the brightness temperature in K. Alt text: LVD (Longitude-velocity diagram) of Arm I by 45m telescope.

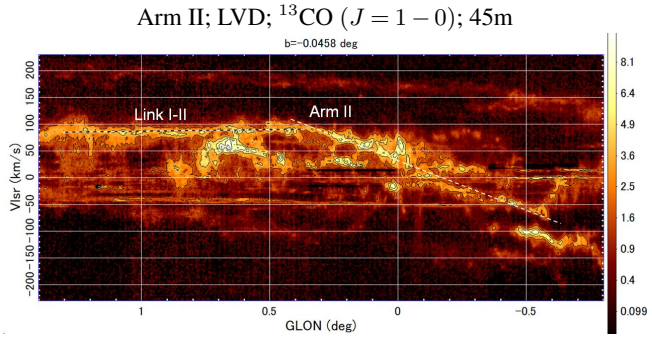

Fig. 2. Arm II on the LVD in ^{13}CO $(J=1-0)$ line by 45m at a representative latitude that is indicated in each panel. Color bars indicate the brightness temperature in K. Alt text: LVD of Arm II by 45m.

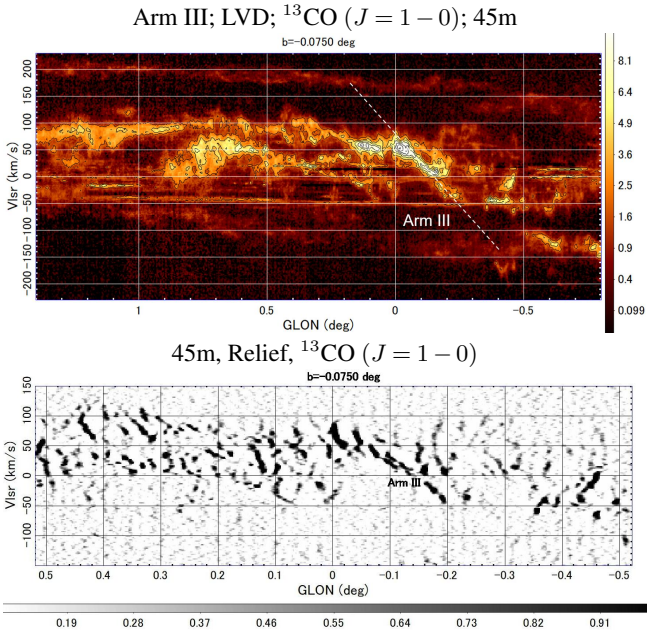

Fig. 3. [Top] Arm III LVD in ^{13}CO $(J=1-0)$ line with 45m at representative latitude $b=-0.^{\circ}075$. [Bottom] Same, but relieved LVD (see Appendix 1 for the relieving method) for the central region. Color bars indicate the brightness temperature in K. Alt text: LVD of Arm III by 45m.

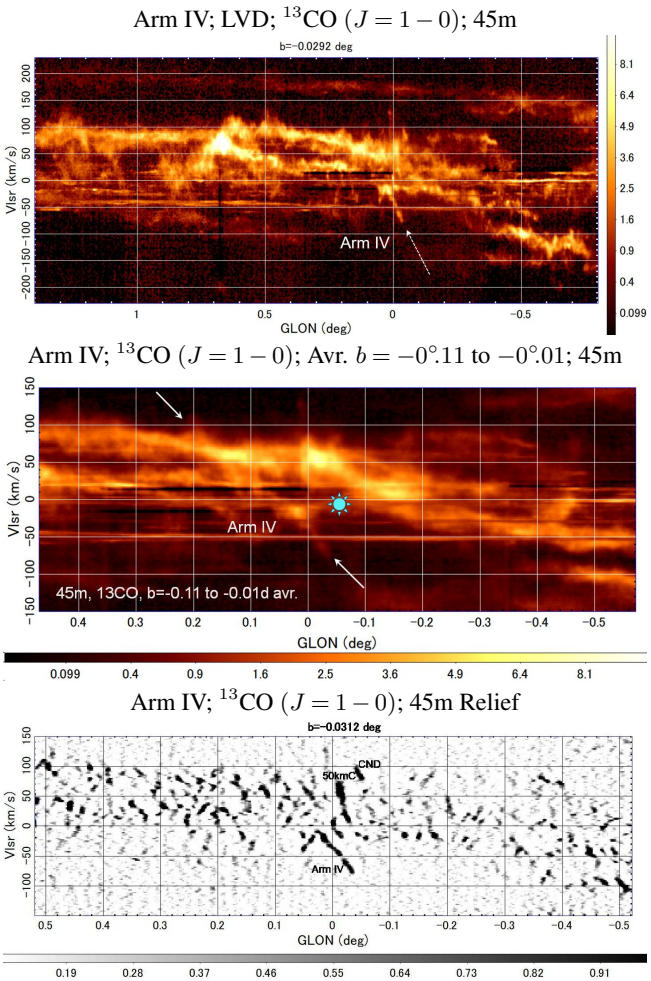

Fig. 4. Arm IV: [Top] LVD in ^{13}CO ($J=1-0$) by 45m at representative latitude, $b=-0.^{\circ}03$. [Middle] LVD averaged between $b=0.^{\circ}11$ and $-0.^{\circ}01$, showing the entire arm including positive-velocity extension. [Bottom] Relieved LVD at $b=-0.^{\circ}03$, showing negative velocity ridge. Color bars indicate the brightness temperature in K. The blue symbol is Sgr A*. Alt text: LVD of Arm IV by 45m.

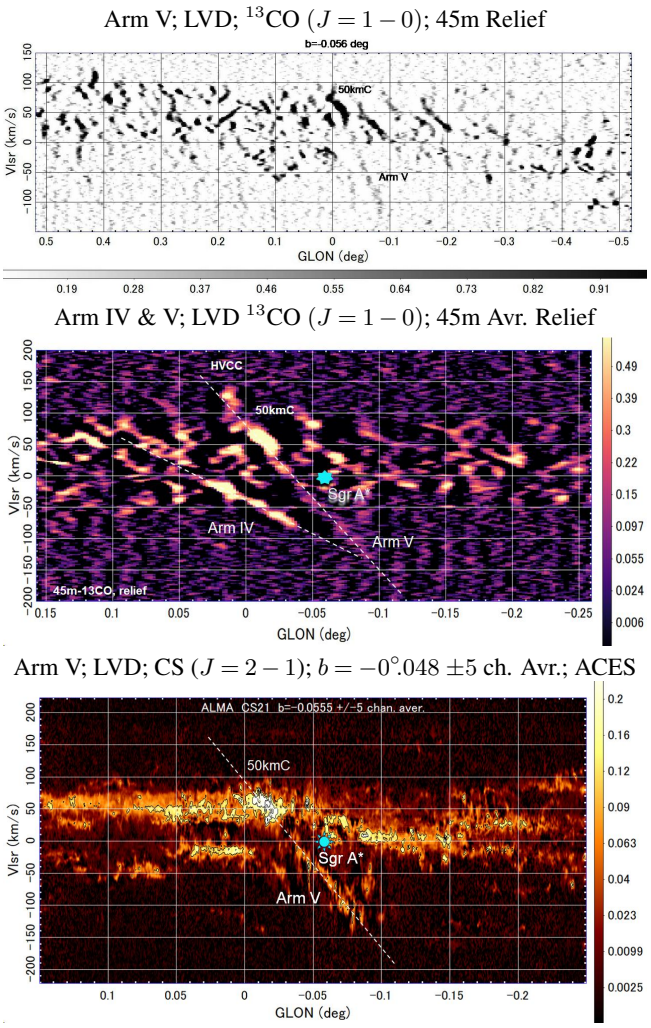

Fig. 5. Arm V: [Top] LVD in ^{13}CO ($J=1-0$) by 45m at representative latitudes $b=-0.^{\circ}056$ by relieved LVD. [Middle] Same, but averaged between $-0.^{\circ}1$ to 0°. [Bottom] LVD averaged over ±5 (±4 km s^{-1}) channels around $b=-0.^{\circ}0555$ in CS ($J=2-1$) by ALMA. Alt text: LVD of Arm V by 45m.

or the "LV-masking function",

$$f(l, v_{\rm LSR}) = \exp\left[-\left(\frac{v_{\rm LSR}-v_{\rm ridge}(l)}{\delta v}\right)^2\right]. \quad (1)$$

Here, $v_{\rm ridge}(l)$ represents $v_{\rm LSR}$ of the LV ridge at longitude l, and is expressed by a linear or a bent-linear (curved) function of l to represent the dashed line of each arm in figures 1 to 7. So, in most cases

$$v_{\rm ridge}(l) = Al + B, \quad (2)$$

where $A = dv_{\rm LSR}/dl$ and $B = v_{l=0^\circ}$ and are taken to be constants, and were measured along each of the dashed lines in figure 1 to 7. The velocity half width was estimated to be $\delta v = 10$ and 7.5 km s^{-1}for ^{13}CO ($J=1-0$) and CS ($J=2-1$), respectively, using LVDs around the clearest parts of Arms I to III (figures 1 to 3), and Arms IV and V (figures 4 and 5).

The obtained moment 0 maps along LVR from 45-m in ^{13}CO ($J=1-0$) and from ALMA in CS ($J=2-1$) and H^{13}CN ($J=1-0$) are shown in figures 9 and 10, respectively. The vertical broad and bright bands in the maps of Arms IV to VI from ALMA are contamination of the local disc and the "fore-/background CMZ" including a part of Arm I and II.

3 Galactic-Centre Arms

The so far identified Arms I to VI are summarized in the LVD of figure 7 by the dashed lines. In this section we describe the individual arms based on the LVDs as well as the LV-masked moment 0 maps. We highlight the inner Arms III and IV, and report the existence of a new arm, which we name Arm V. We further identify an even inner arm, naming it Arm VI, which is an alternate view of the circum-nuclear disk (CND) (Wright et al. 2001; Tsuboi et al. 2018). We also discuss the mini-spirals around Sgr A* (Tsuboi et al. 2017), which we consider to compose the innermost family of the arms, and thus name Arm VII.

3.1 Arm I

Arm I, or the Sgr-B Arm, appears as the most prominent LV ridge of the CMZ, and is considered to be a spiral arm or a ring on

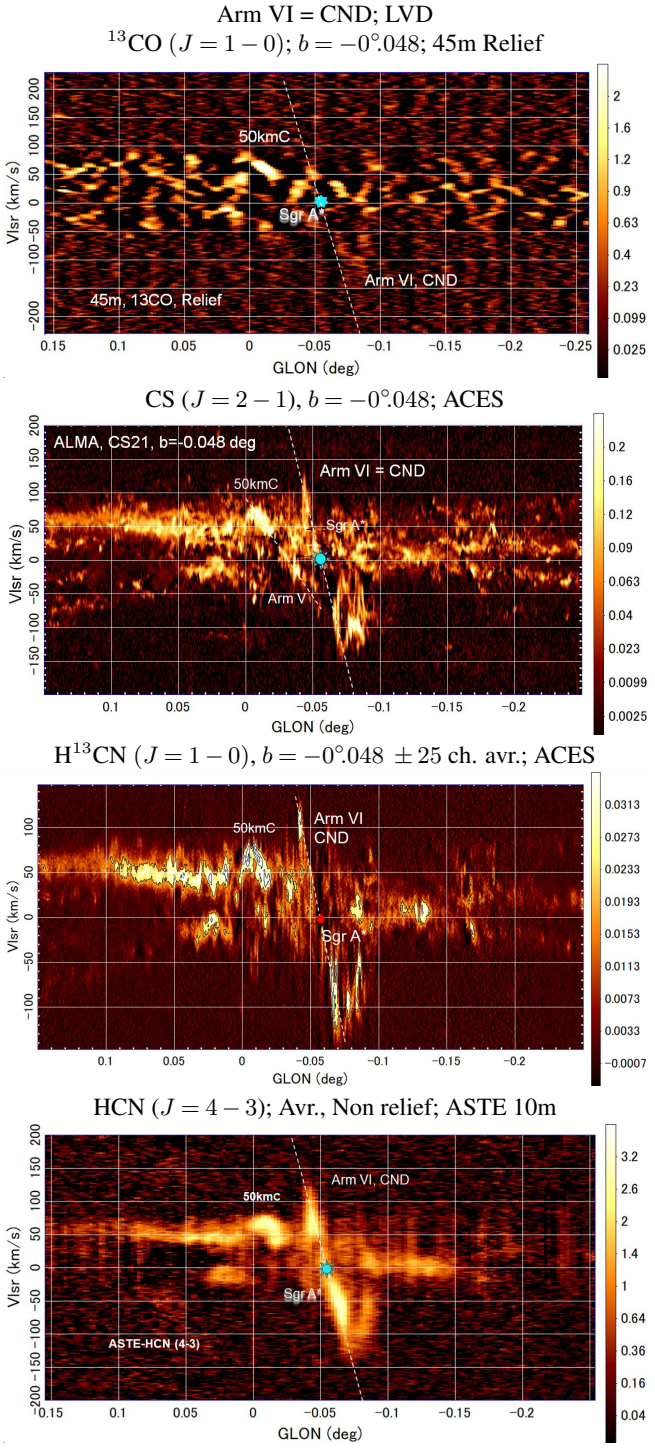

Fig. 6. Arm VI: [Top] 45m LVD (relief) in ^{13}CO ($J = 1 - 0$) at $b = -0°.048$. [2nd] ALMA CS ($J = 2 - 1$) LVD. [3rd] ALMA H^{13}CN ($J = 1 - 0$) LVD. [Bottom] ASTE H^{13}CN ($J = 1 - 0$) LVD. Color bars indicate the brightness temperature in K for top panel (45m) , and in Jy beam^{-1} for others (ACES). Alt text: LVD of Arm VI by 45m.

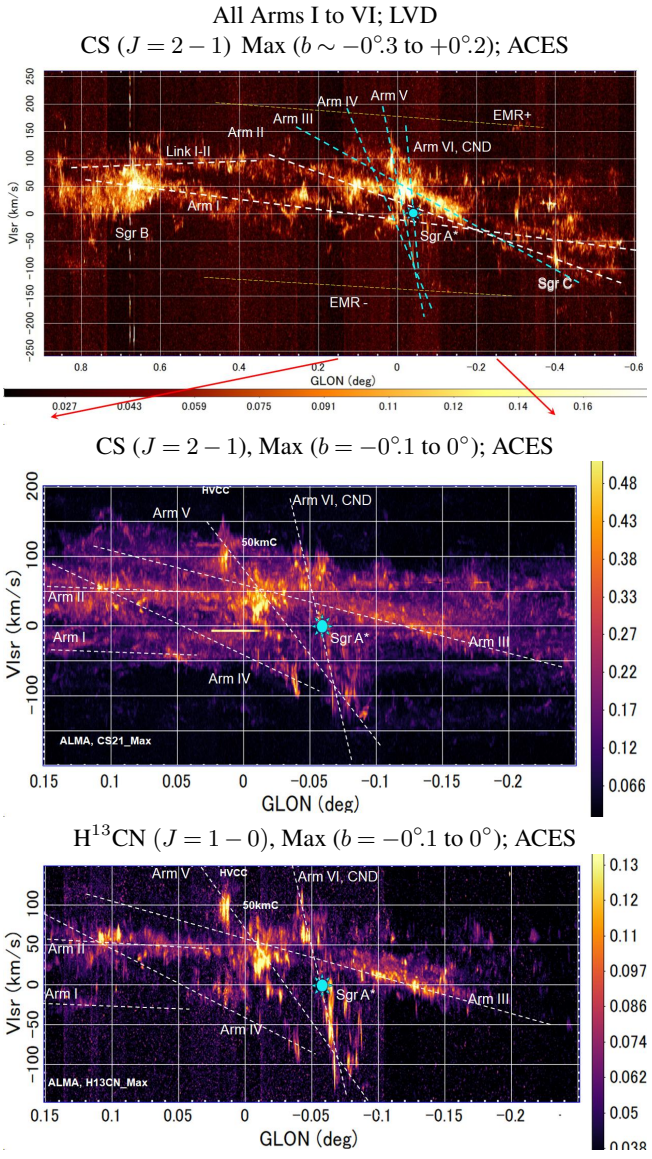

Fig. 7. [Top] LVDs in maximum (peak) intensity along each latitude in CS ($J = 2 - 1$) by ACES. The identified Arms are shown by dashed lines in the entire ACES field ($b \sim -0°.3$ to $+0°.2$). EMR stands for expanding molecular ring (+/- for positive and negative $v_{\rm LSR}$, respectively). Arm III shows up most clearly in this diagram. [Middle] Same, but the central region. [Bottom] Same, but in the H^{13}CN ($J = 1 - 0$) line. Color bars indicate the intensity scale in Jy beam^{-1}. Alt text: LVDs of Arm I to VI by ACES.

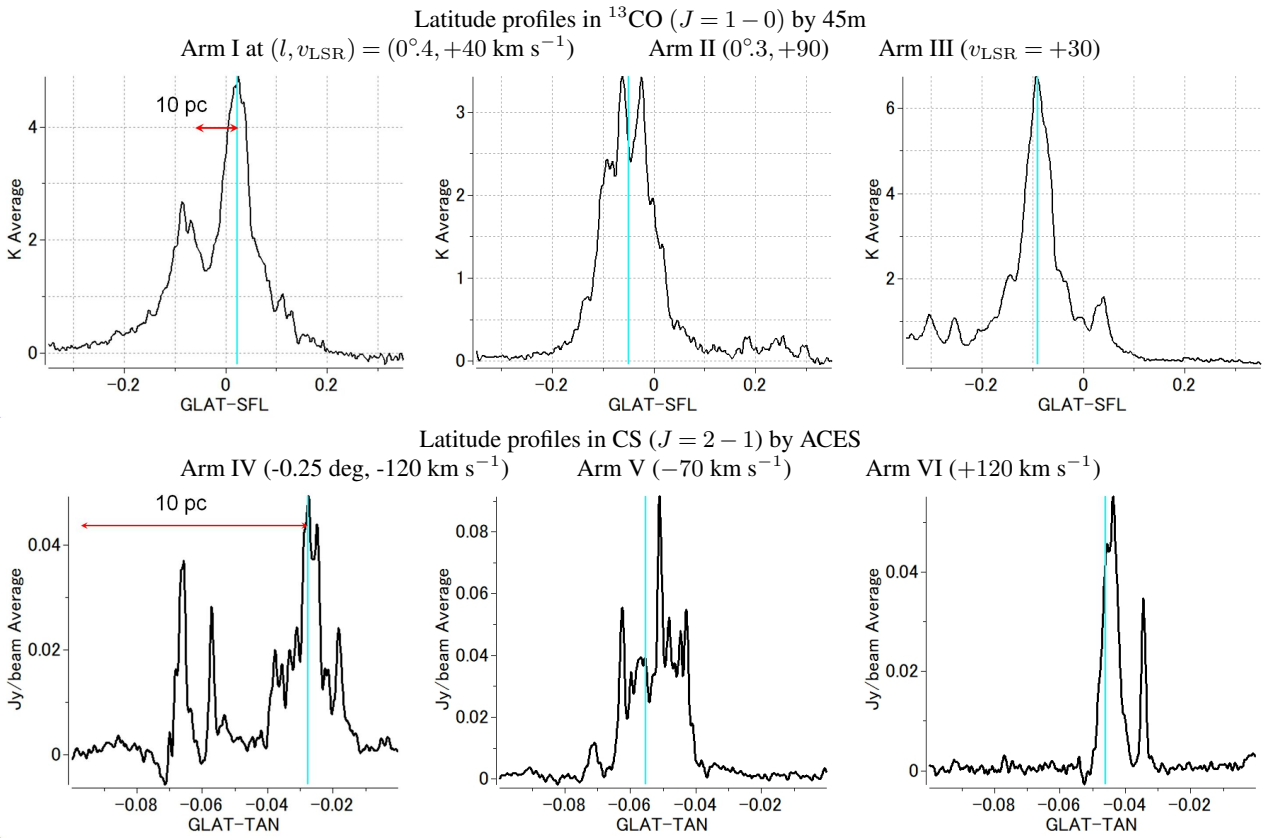

Fig. 8. Latitudinal profiles in ^{13}CO ($J = 1 - 0$) line emission of Arm I to III from 45 m (top panels) and CS ($J = 2 - 1$) of Arm IV to VI from ACES (bottom panels) at representative longitudes and velocities on the arm ridges in LVDs. The vertical blue lines indicate the latitudes at which the arms show up most clearly in the LVDs. The arm's full b width z was measured at ~ 20% level of maximum. Note that the latitude range is $0^\circ.6$ for Arms I to III, while $0^\circ.1$ for IV to VI, and the significant decrease of the width toward Sgr A*. Red arrows indicate 10 pc. Alt text: Latitude profiles of Arm I to VI.

the nearer side of Sgr A*, the Milky Way's nucleus. Moment 0 maps of this arm shown in panels (A) and (B) of figure 9 reveal a long and sharp arm tailing from the Sgr B cloud complex. Active star forming regions Sgr B1 and B2 are located on this arm (Sofue 1995; Sofue 2022; Oka et al. 1998; Tokuyama et al. 2019; Henshaw et al. 2016; Henshaw et al. 2023).

3.2 Arm II

Arm II, or the Sgr-C Arm, is the second-brightest arm associated with Sgr C, and is rotating on the far side of Sgr A. Arms I and II are linked by a horizontal LV belt (Link I-II) as indicated by the dashed line in figure 7.

Link I-II appears to be connected to the more outer disc at velocities at $v_{\rm LSR} \sim 100$ km s^{-1}, which may suggest a gaseous arm connecting the CMZ and the Galactic disc. However, we do not discuss this feature in this paper, because it is far outside the ACES field.

In panel (C) of figure 2 we show a moment 0 map integrated along the bent LVR Arm II and Link I-II (figure 2). This map indicates that Arm II is tailing from Sgr C and extends nearly symmetrically to Arm I from Sgr B, and extends further to the west along the horizontal LVR Link I-II beyond the edge of Arm II. Panel (D) presents a part of Arm II in the moment 0 map traced by the tilted straight LVR alone.

The molecular gas mass of the CMZ is shared mostly by these two main Arms I and II as discussed below in section (4.5). The two arms have been proposed to compose the main 120-pc ring (Sofue 1995) of the CMZ, and have been extensively studied in order to derive the 3D structure of the CMZ (Molinari et al. 2011; Kruijssen et al. 2015 ; Henshaw et al. 2016; Tokuyama et al. 2019; Sofue 2022). It is further suggested that the Arms are related to the outer star-formation region Sgr E ($l \sim -1^\circ$) and supernova remnants Sgr D ($\sim +1^\circ.2$), drawing a double infinity ($\infty\infty$) on the sky (Sofue 2022). However, the degenerate Arms I and II are resolved in the LV space, and the masked moment 0 map (figure 9) shows a simple tilted ring.

3.3 Arm III

Arm III has not been studied in detail so far in spite of its high brightness. It is visible in ^{13}CO ($J = 1 - 0$) in the LVD in figure 3 and in the moment 0 maps in figures 9 and 10. The LV ridge of this arm is composed of two parallel stripes in H^{13}CN ($J = 1 - 0$) and HCN ($J = 4 - 3$) lines. The line spectrum shows a clear center-velocity absorption along this arm as shown by an insertion in panel E of figure 9. The absorption belt along Arm III will be discussed in some detail later in subsection 5.3.

This arm seems to consist of the GMC M-0.13-0.08 (20kmC) (see Takekawa et al. (2017a)). The moment 0 map in figure 3 shows a rather short arm on the sky, being led by a bright clump of 20kmC. If the 20kmC is physically associated with Arm III, its 3D position can be determined kinematically, as will be done in section 4.1. Thereby, we assume that Arm III is in front of Sgr

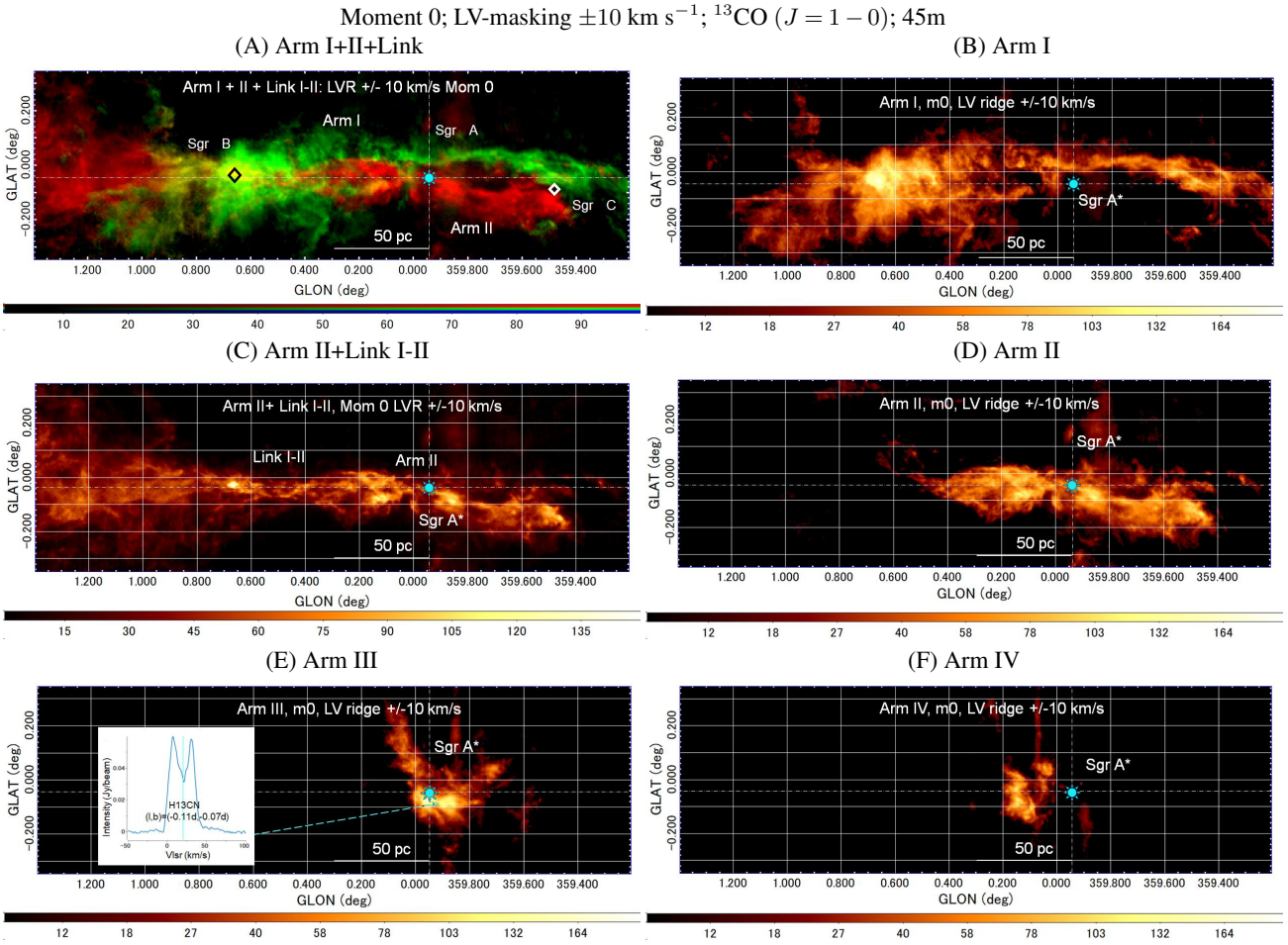

Fig. 9. Integrated intensity (moment 0, [K km s^{-1}]) maps in ^{13}CO $(J = 1 - 0)$ line about LVR for ± 10 km s^{-1}of the GC Arms from Nobeyama 45 m at a resolution of $16.7''$. (A) Arm I (green) + II + Link I-II (red); (B) Arm I; (C) Arm II + Link I-II along the bent LVR in figure 2; (D) Arm II (straight LVR alone); (E) Arm III; and (F) Arm IV. The color bars indicate the integrated intensity (moment 0) in K km s^{-1}. A H^{13}CN $(J = 1 - 0)$line spectrum of Arm III at $(l, b) = (-0^\circ.11, -0^\circ.07)$ is inserted in panel (E). Alt text: Moment 0 maps using masked LVDs for Arms I to III by 45m.

A*, following the face-on geometry proposed by Takekawa et al. (2017a).

However, it has also been suggested that there is a physical contact between the +20-km s^{-1} cloud and the CND (Takekawa et al. 2017a). If this is the case, a different view is required, and Arm III may be re-defined as a long bright ridge only in negative $v_{\rm LSR}$, extending to $(l, v_{\rm LSR}) \sim (-0^\circ.2, -50$ km s$^{-1})$.

Another concern is its possible relation to the 50kmC: As shown in the relieved LVD in figure 3, the 50kmC is located on the increasing-longitude extension of Arm III. In this paper, however, we argue that the 50kmC is more reasonably associated with Arm V not only for the LV position but also for the large dv/dl value close to that of Arm V, as will be discussed in subsection 3.5.

Line-of-sight locations of 20- and 50kmC will be mentioned later in subsection 5.3.

3.4 Arm IV

Arm IV is the most clearly visible arm in the relieved ^{13}CO $(J = 1 - 0)$ LVD at negative $v_{\rm LSR}$ as shown in the bottom panel of figure 4. Its positive-$v_{\rm LSR}$ extension is visible in the original LVD as indicated in the middle panel of this figure, but is strongly disturbed by the contamination from Arms I and II as well as the extended CMZ emission.

This arm can be clearly traced on the LVD in figure 4, and is also visible in the moment 0 map in CS $(J = 2 - 1)$ from ACES. The arm runs westward from $l \sim 0^\circ.02$ and stops at $l \sim -0^\circ.04$.

A part of this Arm has been identified as "C1" clump at $(l, b, v_{\rm LSR}) \simeq (-0^\circ.03, -0^\circ.06, -70$ km s$^{-1})$, which shows intense CS emission (Oka et al. 2011).

3.5 Arm V: tilted ring and 50kmC

Arm V is a straight and long LV ridge composed of a low-brightness stripe extending from $(l, v_{\rm LSR}) = (-0^\circ.02, +30$ km s$^{-1})$ to $(-0^\circ.1, -130$ km s$^{-1})$, as shown in figure 5.

As the LVDs in figure 5 indicate, the 50kmC is located exactly on the positive-velocity extension of Arm V. Moreover, the velocity gradient of 50kmC is about equal to that of Arm V, which will be discussed in section 4.1. The LV behavior suggests that the 50kmC and Arm V compose a single arm rotating on the same orbit.

The moment 0 Arm V in CS $(J = 2 - 1)$ (figures 10 (C)) runs nearly horizontally but inclined along position angle PA $\sim 25^\circ$, extending from or contacting with the 50kmC to the west. It seems to

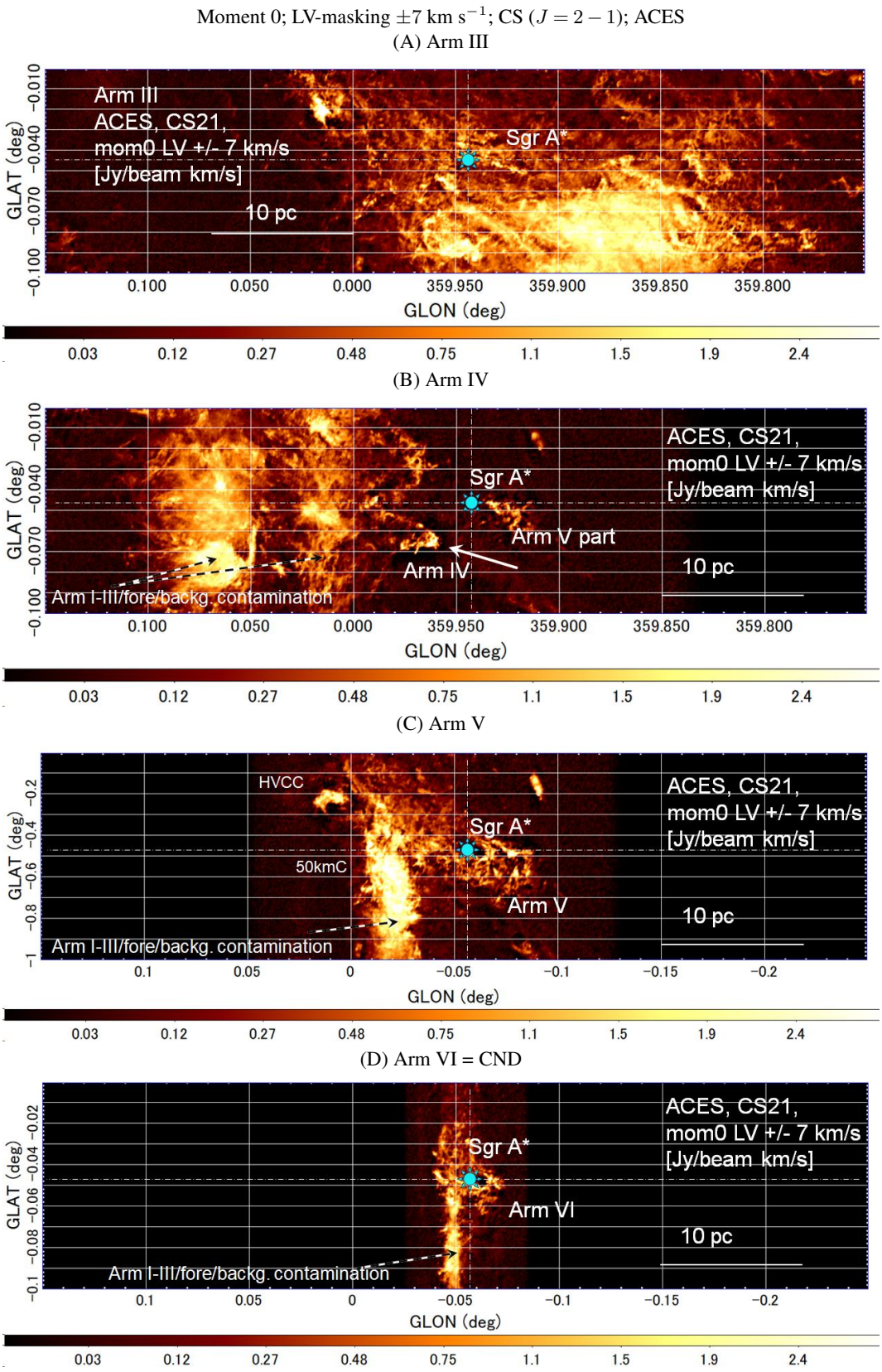

Fig. 10. ACES CS ($J = 2 - 1$) integrated intensity (Moment 0; [Jy beam^{-1}km s^{-1}]) along LV ridges with $\delta v = \pm 7.5$ km s^{-1}for Arm III to VI (CND) at a resolution of $2.2''$. Vertical broad bands are contamination of the extended emission of CMZ and Arms I and II. Color bars indicate the integrated intensity (moment 0) in Jy beam^{-1} km s^{-1}. Alt text: Moment 0 maps using masked LVDs for Arms IV to VI by ACES.

compose an elliptical ring of axial ratio $b/a \sim 0.25$, or inclination angle of $i \sim 76^\circ$. However, the ellipse is not perfectly continued to the 50kmC that appears as a broad and bright cloud.

It is interesting to point out that the high-velocity compact cloud (HVCC) G0.02-0.02 at $v_{\rm LSR} \sim 100$ km s^{-1}(Oka et al. 1999; Takekawa et al. 2017b; Oka et al. 2022; Iwata et al. 2023) is apparently aligned on the straight extension of Arm V in the LVD in the positive-$v_{\rm LSR}$ direction . Also, in the moment 0 map (figures 10), it lies in the western extension of the major axis of the Arm-V ellipse, drawing a bright arc concentric to the ellipse.

Extensive studies of the central molecular clouds have argued that the 50kmC composes a more extended complex including 20kmC (Tsuboi et al. 2009; Uehara et al. 2019). Also, the HVCC CO 0.02-0.02 has been considered to be an isolated compact object (Oka et al. 1999; Takekawa et al. 2017b; Oka et al. 2022; Iwata et al. 2023). Therefore, the association of 50kmC and HVCC with Arm V is controversial at the moment. We will touch upon on these features again in subsection 5.3.

We also comment that the millimeter ultra-broad line object (MUBLO) G0.02467-0.0727 with the centroid $v_{\rm LSR} \sim 40$–50 km s^{-1}(Ginsburg et al. 2024) is located near the longitude of the HVCC in the tangential direction of the Arm-V ellipse. However, MUBLO is displaced to the south by $-0^\circ.05$ (~ 7 pc) and ~ -50 km s^{-1}in radial velocity, so that it may not be related to Arm V.

3.6 Arm VI - CND: tilted ring with trailing fins

The CND (Wright et al. 2001; Montero-Castaño et al. 2009; Martín et al. 2012; Tsuboi et al. 2018; Hsieh et al. 2021) is recognized in the CS ($J = 2-1$) and H^{13}CN ($J = 1-0$)-lines in the LVDs in figure 6 as a highly-tilted bright ridge extending from $(-0^\circ.04, +120$ km s$^{-1})$ to $(-0^\circ.07, -130$ km s$^{-1})$ indicating a rotating ring. We call this ring Arm VI, which is equivalent to CND.

We stress that the arm is hardly visible in the ^{13}CO ($J = 1-0$) line, becoming clearer in the LVDs of CS ($J = 2-1$), H^{13}CN ($J = 1-0$), and HCN ($J = 4-3$). This demonstrates that the molecular gas in the CND (Arm VI) is much denser and warmer compared to the general CMZ clouds such as in Arms I and II. The LV ridge exhibits a double-peaked rotating ring structure whose central part is missing due to absorption of molecular lines against continuum emission of Sgr A*. A curved spur is extending from the negative-velocity end of Arm VI, indicating that the arm is associated with a high-velocity non-circular flow, which will be touched upon in later subsection 5.5.

Figure 11 shows moment 0 maps of Arm VI in CS ($J = 2-1$) and H^{13}CN ($J = 1-0$) as integrated within $\delta v_{\rm LSR} = \pm 7$ and ± 10 km s^{-1} from the LV ridge (LVR), respectively, which are in good agreement with the CS ($J = 7-6$) map using ALMA by Tsuboi et al. (2018). The figure exhibits an elongated ellipse centered on Sgr A* as marked by the dashed line in the bottom panel of figure 11, which has an axial ratio of $b/a \sim 0^\circ.0085/0^\circ.023 = 0.405$ at position angle of the major axis of PA$\sim 70^\circ$. If it is a circular ring, the inclination angle is $i \simeq 66^\circ$. Several spiral arms and fins are bifurcating from the ring, trailing in the sense of counter-clockwise rotation in the figure (on the sky).

The positive-latitude side of the ring (north wing) is missing, which may also be attributed to absorption of Sgr A's continuum. On the contrary, the negative-latitude side (south wing) is not absorbed, drawing a nearly perfect ellipse. The orientation of absorption feature indicates that the northern wing of the ring is in front of Sgr A and the southern half is beyond it. This is consistent

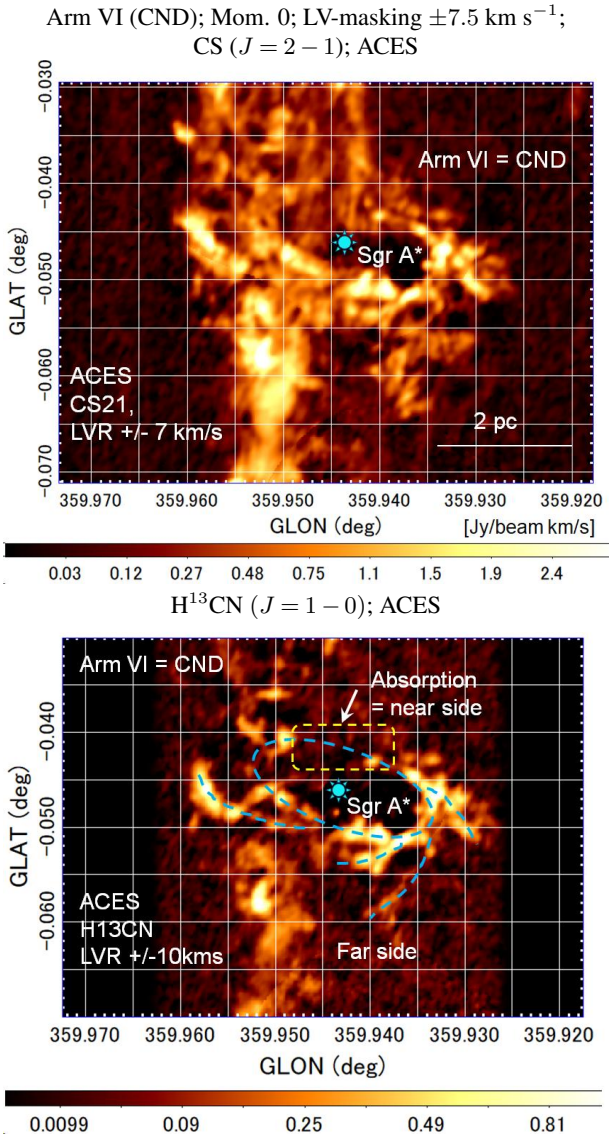

Fig. 11. [Top] Same as figure 10 for Arm VI, but close up . [Bottom] Same, but in H^{13}CN ($J = 1-0$). An ellipse is seen associated with many spiral fins, indicating a ring with inclination angle $i \sim 65^\circ$. Vertical broad bands are contamination of extended CMZ gas and Arms I and II. Alt text: Masked moment 0 maps of Arm VI in CS ($J = 2-1$) and H^{13}CN ($J = 1-0$) by ACES.

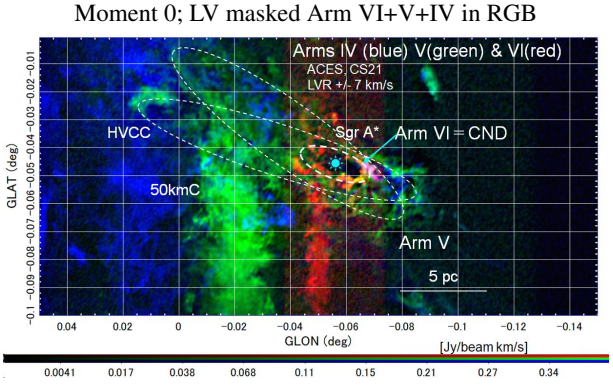

Fig. 12. Overlay of Arms IV, V and VI in blue, green and red colors, respectively. Arm V draws two inclined circles as marked by the two large dashed ellipses with diameters of ~ 16 pc. The small ellipse indicates Arm VI (CND). Alt text: Overlay of Arm VI+V+IV moment 0 maps in RGB colors.

with the counter-clockwise rotation of the disc seen from below the Galactic plane. There is a hole in the center of the ring coinciding with Sgr A*, which is due to the absence of molecular gas around the minispiral at high temperature as well as due to absorption of Sgr A's continuum emission.

In figure 12 we show an overlay of Arms IV, V and VI in blue, green and red colors, respectively, in order to demonstrate their geometrical relationship on the sky and the differences in sizes. Possible elliptical features found in the previous subsections are marked by the dashed lines. One of the outer ellipses of Arm V is drawn to trace the curved arc of the HVCC. The two ellipses of Arm V are considered to represent inclined circular rings of diameters of ~ 16 pc projected on the sky, whose radius is measured to be $R \sim 8.2$ pc derived from the dv/dl method (see section 4.1). However, the orbits are eccentric with respect to Sgr A*.

3.7 Arm VII: Minispirals as the seventh arm

The mini spirals of radius $R \sim 1.4$ pc are not detected in the present data as they are composed of ionized gas (Zhao et al. 2009; Tsuboi et al. 2017). We here try to interpret these innermost spirals as an extension of the arm structure in the CMZ, and call them Arm VII. Interestingly, this "Arm" lies on the natural extension of the radius-number and radius-thickness relations discussed in subsection 4.2.

3.8 Fine LV ridges and stripes

Besides the large-scale, grand-designed arm structures that trace as the tilted LV ridges spanning $\sim \pm 100$ km s^{-1} like Arms I to VI, there are numerous fine stripes composed of shorter ($\sim \pm 10$–30 km s^{-1}) vertical LV ridges seen in the relieved LVDs from 45m telescope (Appendix 1, figure 20) and those in the ACES LVDs at higher resolution with $\sim \pm 10$ km s^{-1}(figure 7). They are mostly individual molecular clouds not resolved in the longitude direction, indicating that the CMZ contains numerous clouds with sizes less than the beam width, $\sim 2'' \sim 0.1$ pc and velocity dispersions of ~ 10–30 km s^{-1}).

We point out that some of such LV ridges (individual clouds) are inclined in the same sense as that caused by the Galactic rotation, but generally with tilt angles steeper than those of the main Arms I and II. This suggests that some of the LV ridges, except for the innermost LV ridges discussed in the next section, represent individual clouds locally rotating more rapidly than the disc's rotation due to self contraction with the cloud's angular momentum being conserved.

4 Arm radius and thickness

4.1 Radii of GC Arms using dv/dl method

Here we introduce three observable quantities to describe the identified arms on the LVD: (1) Velocity gradient (slope) dv/dl of the LV ridge, (2) velocity intersection $v^*_{\rm LSR}$ of the ridge at the longitude of Sgr A* at $l = -0.^\circ056$, and (3) peri-/apocentric longitude offset Δl_0 from Sgr A*, at which the motion of gas becomes perpendicular to the line of sight so that $v_{\rm LSR} = 0$ km s^{-1}. Table 1 lists the values of $dv_{\rm LSR}/dl$, $v^*_{\rm LSR}$ and Δl measured by eye-fitting to the corresponding LV ridges in the LV plane.

If we assume that an extended object is rotating around a certain center, the curvature of the flow line, R, is related to the velocity gradient:

$$R \simeq R_0 V_{\rm rot} \left(\frac{dv_{\rm LSR}}{dl} \right)^{-1} \sin\, i\, \cos^{-1} j, \qquad (3)$$

where $V_{\rm rot} \sim 150$ km s^{-1} is the rotation velocity, i is the inclination of orbital plane, and j is the position angle of the rotation axis (Sofue 2006). If we assume that the flow is circular around Sgr A*, the radius is equal to the galactocentric distance R. Hereafter, we adopt this assumption, and denote the galactocentric distance by R. We also assume that the arms are nearly edge-on, $i \sim 90^\circ$ and $j \sim 0^\circ$. The error in the curvature propagates from that in the dv/dl measurement, which is about $\pm 5\%$, and the uncertainty of the rotation velocity, which causes an error of a factor of 1.5 (100–150 km s^{-1}). Therefore, the error of the curvatures/radii of the Arms determined in this paper is a factor of ~ 1.5.

Note that this method measures the local curvature of the streamlines for a given flow velocity. However, if the flow is not circular, or elliptical, hyperbolic, etc., it gives the local streamline curvature. It works even with overlapping expansions (contractions) because $dv_{\rm expa}/dl \simeq 0$ near the rotation axis. Note also that this measures the curvature of the streamlines, but not the curvature of filaments or arms that may be inclined at an angle to the streamlines, like galactic shock waves. Here, streamline means the direction of the flow vector, and filament/arm means the density-enhanced gaseous structure.

In case of Arm IV, for example, we measure the velocity gradient to be $dv_{\rm LSR}/dl \simeq 200$ km s^{-1}per $0.^\circ02$ in the LVDs, yielding $R \simeq 21$ pc, assuming $i \sim 90^\circ$ and $j \sim 0^\circ$. The rotation period is then $P = 2\pi R/V_{\rm rot} \sim 0.86$ Myr.

Table 1 lists the estimated values of R and P for the identified arms. In figure 13 (A) we show the "arm-radius relation", or a plot of radii against arm number I to VII. The plot is approximately fitted by

$$R \sim R_{\rm A} \left(\frac{V_{\rm rot}}{150\ {\rm km\ s^{-1}}} \right) \times (2/5)^N \ {\rm pc}, \qquad (4)$$

(N =I, II, ..., VII) within an error of factor ~ 2, where $R_{\rm A} = 630$ pc. This shows that the existence of the arms is discrete, and that the ratio between the radii of two neighboring arms/rings is ~ 2.5. The relation can be alternatively attributed to a logarithmic spiral with pitch angle of $p \sim 22^\circ$.

4.2 Face-on view of GC Arms

Using the estimated radii of the arms, their orientations in the CMZ are illustrated in figure 14. Panel (A) is a schematic sketch of the proposed edge-on and oblique views of the CMZ. Panel (B) shows the face-on views of the Arms using their calculated radii with dv/dl method, where the longitudinal offset of the nodes at which $v_{\rm LSR} = 0$ km s^{-1}are marked by red lines. Position angles of the associated molecular clouds (Sgr B, C, 20- and 50kmC) with respect Sgr A* calculated by $\theta = \sin^{-1} v_{\rm LSR}/V_{\rm rot}$ ($v_{\rm LSR} = 150$ km s^{-1}) are marked by the dashed lines with the angles. In panel (C) we enlarge the face-on plot with the possible locations of 20- and 50kmC. In this plot Arm III is put on the near side according to the suggested location of 20kmC in front of Sgr A* (Takekawa et al. 2017a). The near vs far problem of the clouds will be discussed in detail in the next section.

The result is globally consistent with the face-on view of the 20- and 50kmC clouds with Sgr B and C as obtained using the intensity ratio of the CO line emission to OH absorption line (Yan et al. 2017).

In figure 13 (panel A) we plot the estimated radii of the Arms against their numbers I to VII (1 to 7). The arm radius is represented by a relation, $R \sim 630 \times (2/5)^N$ pc, with an error of a factor ~ 2. This suggests a pseud-Bode's law or a logarithmic spiral of pitch angle $p \sim 22^\circ$.

Table 1. Parameters of the GC arms inferred from dv/dl method[#].

Arm	dv/dl ($\mathrm{km\,s^{-1}\,deg^{-1}}$)	Δl (deg)	$v^*_{\rm LSR}$ ($\mathrm{km\ s^{-1}}$)[##]	$R(V_{\rm rot})$ (pc) ($100\ \mathrm{km\,s^{-1}}$)	$R(V_{\rm rot})$ (pc) ($150\ \mathrm{km\,s^{-1}}$)	P (Myr) ($150\ \mathrm{km\,s^{-1}}$)	$z_{\rm full}$ (pc)	$\hat{i}$ (deg)	$\mathrm{Vol}_i/\mathrm{Vol}_{\rm I+II}$ (deg)
Arm I	150.	$+0.25$	-40	94.	141.	5.9	26	4	1.0
Arm II	212.	-0.1	$+10$	67.	101.	4.2	20		–
Arm III	507.	-0.1	$+50$	28.	42.	1.7	4.7		$\sim 2\times10^{-2}$
$\supset$20kmC	440[††]								
Arm IV	1020.	$+0.08$	-80	14.	21.	0.86	3.6		$\sim 3\times10^{-3}$
Arm V	2600.	$+0.025$	-50	5.4	8.2	0.34	3.1	14	$\sim 4\times10^{-4}$
$\supset$50kmC	~ 3000	—	—	—					
Arm VI	9300.	0	0	1.5	2.3[†]	0.1	1.4	24	$\sim 10^{-5}$
$\equiv$ CND									
Arm VII	10^4	0	0	~ 1.4[‡]	<=	~ 0.1	~ 1	34	
$\equiv$ minispirals									

[#] Inclination angle is assumed to be $i \simeq 90^\circ$ (tilt ange $\hat{i} = 0^\circ$), except for Arm VII.
[##] $v^*_{\rm LSR}$ is $v_{\rm LSR}$ at $l = -0^\circ.056$ (Sgr A*). The reference center is taken at Sgr A* with $(l, b) = (359^\circ.944227, -0^\circ.046157)$.
[††] Read from LVD of Takekawa et al. (2017a).
[†] Consistent with the current measurement $R \simeq 2.5$ pc (Tsuboi et al. 2018).
[‡] Taken from the current map in recombination line (Zhao et al. 2009).

We have so far assumed that the orbits of the arms are circular around a center at the longitude at which the LV ridge crosses the $v_{\rm LSR} = 0$ km s^{-1}line. Although this assumption leads to a reasonable galactocentric distance R using the dv/dl method, in order to map the arms and clouds more precisely, we need a realistic gravitational potential and a flow line model around Sgr A (e.g. Kruijssen et al. 2015 (); Kruijssen et al. (2019)), which is, however, beyond the scope of this paper (see further discussion in section 5).

4.3 Vertical thickness decreasing toward nucleus

In section 2.5 we have shown that the vertical thickness of the Arms increases with the radius R. In figure 13 (B) we plot the full thickness z of the Arms against galactocentric radius R. Here, we also plotted the supposed vertical extent of the minispiral (Arm VII) of ~ 1 pc from the literature. In this log-log plot, the thickness is approximately expressed by a straight line given by

$$z \sim 0.7(R/1\ \mathrm{pc})^{0.7}\ \mathrm{pc}. \quad (5)$$

If the arm's thickness represents that of the disc, this plot indicates that the thickness of the CMZ disc increases with radius R. It means that the disc inside Arms I and II becomes thinner from a few pc to ~ 1 pc near Sgr A.

Note, however, that these latitude profiles do not include such clouds as the Sgr B complex in Arm I and 50kmC in Arm V, which extend more vertically than expected from the R-z relationship. This raises the question of whether these clouds are physically associated with the arms and how such vertical protrusions could have formed from the thin arms. Alternatively, such "high-z" clouds may manifest large bent (oscillation) of the trajectories or more deviated inclination of orbits from $i \sim 90^\circ$.

We also point out that the vertical thickness of the 200-pc expanding molecular ring (EMR) ($2h_z \sim 150$ pc) at radius ~ 200 pc (Sofue 2017) deviates significantly from the fit to the Arms, as shown by a large cross in figure 13. This will be touched upon in later subsection (5.6).

4.4 Tilt angle of disc increasing toward nucleus: Warping CMZ

As shown in the moment-0 maps (figures 9 and 10), the 120 pc ring consisting of Arms I + II, Arm V, and Arm VI (CND) exhibit elliptical structures on the sky, indicating that the rings deviate significantly from the edge-on orientation. Arm III does not appear as a clear ellipse, but its ridge is tilted a few degrees from the horizontal, which may represent a tilt of the ring. Arm IV is too divergent in the moment-0 map to define a corresponding ellipse. The minispiral (arm VII) is well known for its highly tilted orientation with a minor to major axis ratio of $b/a \sim 0.5$.

We then calculate the "tilt angle" $\hat{i} = 90^\circ - i$ of the ring's rotation axis from the Galaxy's rotation axis. The inclination is measured using the ratio of the minor and major axes of an ellipse. Plotting the results in the last panel of figure 13, we see that the tilt angle increases rapidly with decreasing radius towards the nucleus.

This behavior can be explained in terms of the gas accretion caused by the galactic shock wave as follows: The angular momentum A_z of the gas about the rotation axis is effectively transferred by the oval motion in the barred potential, while the perpendicular component of the angular momentum A_x is conserved. This causes rapider loss of A_z than A_x until the radius becomes comparable to the z thickness, when A_z becomes comparable to A_x, as observed in the central region with Arms V to VII. The magnetic twisting mechanism (Shibata & Uchida 1986) may work similarly, which acts to transfer the angular momentum of a rotating gas disc penetrated by strong vertical magnetic field (Heywood et al. 2022).

4.5 Relationship of the Arms to the general CMZ structure

We next estimate the relative luminosity ($\sim$mass) of the GC Arms to that of Arm I using the arm radii R in table 1 and their vertical thickness z. Assuming about the same molecular-line brightness (within an order of magnitude), the relative luminosity of Arms to that of Arm I is estimated by

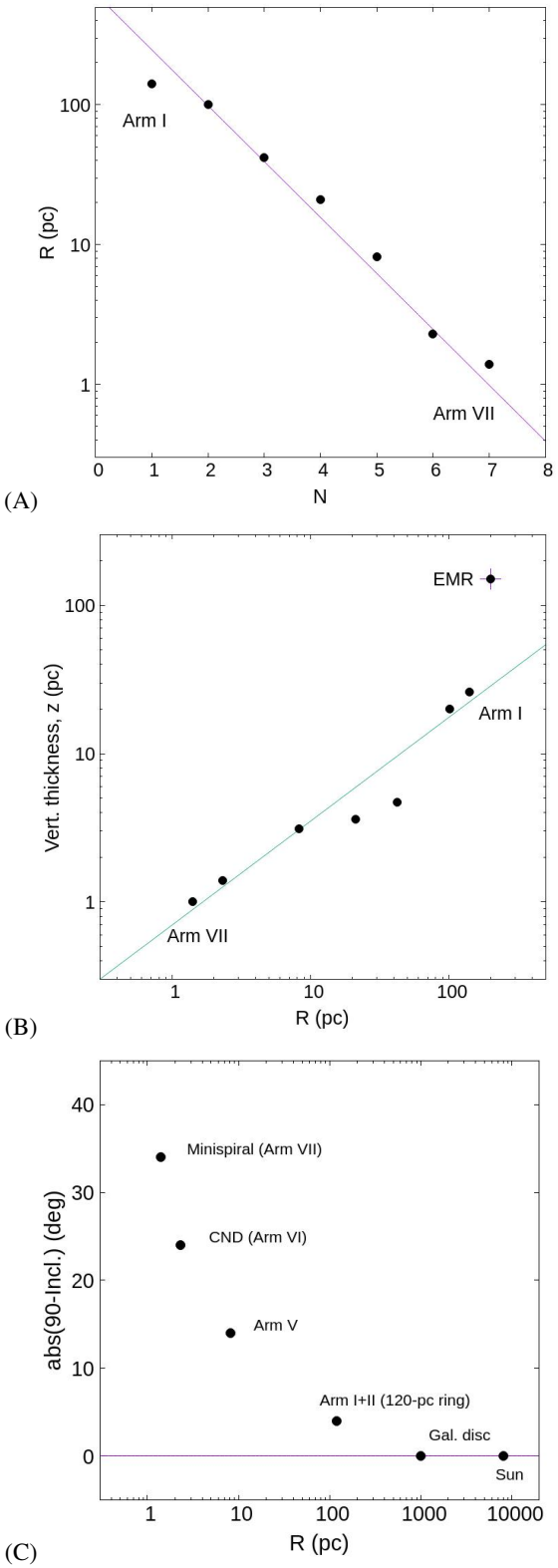

Fig. 13. (A) Arm radius-to-number relation, which is expressed by $R \sim 630 \times (2/5)^N$ pc with an error of factor ~ 2, suggesting a pseud-Bode's law or a logarithmic spiral of pitch angle $p \sim 22°$. (B) Vertical full thickness z of Arm VII (bottom left) to Arm I (top right) plotted against radius R. The straight line represents $z = 0.7(R/1\ \mathrm{pc})^{0.7}$ pc. The point with big cross indicates EMR. (C) Absolute values of $90° -$inclination angle of the arms/rings against radius.) Alt text: Plots of radius vs Arm number, thickness vs radius, and tilt angle vs radius.

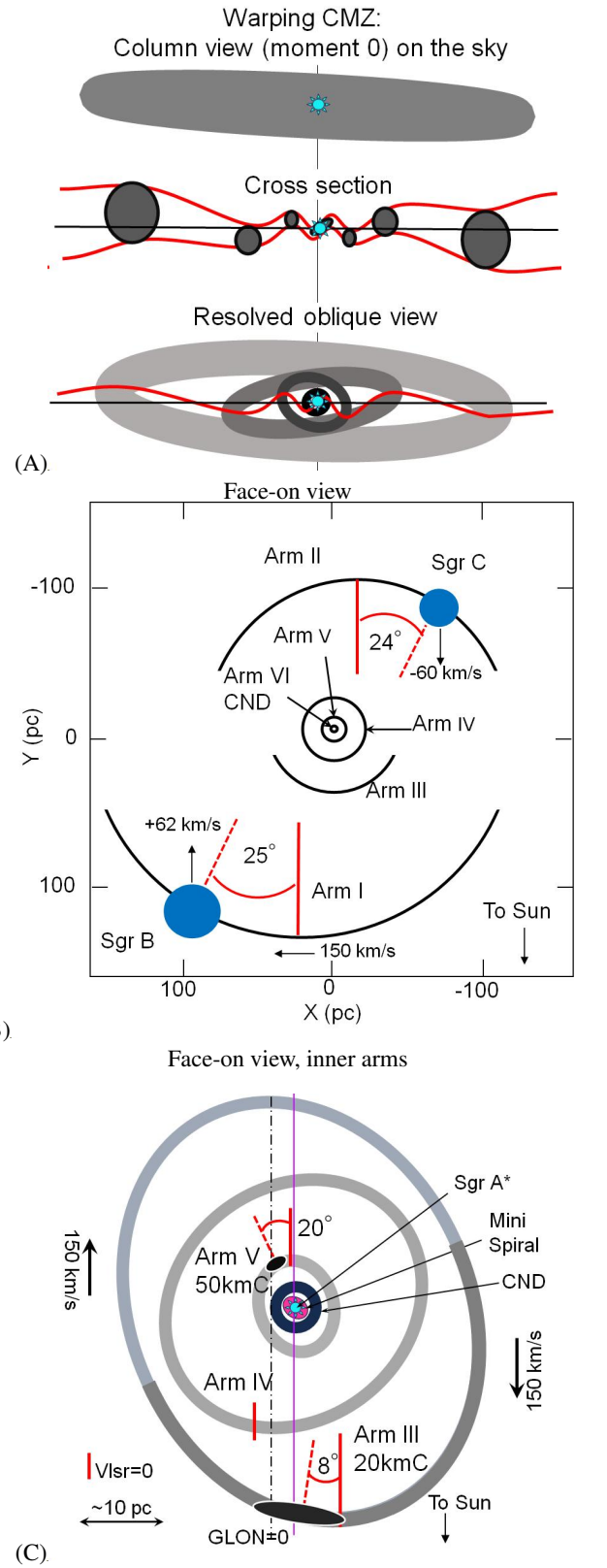

Fig. 14. Schematic illustration of the GC Arms: (A) Projected view of CMZ on the sky, cross section of warping arms, and an oblique view of kinematically resolved arms/rings. (B) Face-on Arms with the radii determined by the dv/dl method. Vertical red bars indicate the nodes of $v^*_{\mathrm{LSR}} = 0$ km s^{-1}, and dashed red lines show position angles $\theta = \sin^{-1}(v_{\mathrm{LSR}}/V_{\mathrm{rot}})$ of Sgr B and C with respect to the curvature centre. (C) Inner arms and locations of 20kmC and 50kmC with their θ. Alt text: Schematic illustrations of the GC Arms.

$$L_i/L_{\rm I} \sim (R_i/R_{\rm I})(\delta R_i/\delta R_{\rm I})(z_i/z_{\rm I}) \sim (R_i/R_{\rm I})^2(z_i/z_{\rm I}), \quad (6)$$

where i stands for the arm number, I to VII, and δR_i is the arm width, which is assumed to be one tenth of the radius, $\delta R_i/R_i \sim 0.1$. We obtain the ratios to be $L_i/L_{\rm I} \sim 1$ (for Arm I, II); $\sim 2 \times 10^{-2}$ (III); $\sim 3 \times 10^{-3}$ (IV); $\sim 4 \times 10^{-4}$ (V); and $\sim 1.4 \times 10^{-5}$ (VI).

Arms I and II share most of the mass of CMZ, composing the 120-pc molecular ring (or the "great ring"). Inside the ring the disc shares only a small portion of the CMZ's volume due to the decrease both in radius and thickness, or Arms III to VI share two orders of magnitudes smaller portion of the entire volume, hence the mass. This is consistent with the low infrared extinction in the nuclear stellar disc (Nogueras-Lara 2022).

The small volume (mass) of the disc inside Arm I and II means that the inflow from the CMZ ring into the nucleus is extremely slow, in other words, the ring is large enough to supply the inner arms, albeit with very low efficiency.

5 Discussion

5.1 General remarks

Henshaw et al. (2023) published a thorough review of recent progress in the study of 3D molecular gas distribution of the CMZ in the $(l, b, v_{\rm LSR})$ space (see the literature therein). There seems to be a consensus that Arms I and II constitute the main structure of the CMZ, composing a large ring-like structure (the 120-pc ring) of radius $\sim$ 100-120 pc rotating clockwise around Sgr A* as seen from the North Galactic Pole.

However, apart from some mentions of the existence of Arms III and IV, there has been no detailed study of the spiral arm or ring structure within the 120-pc ring. In this paper, we showed that there are many more inner arms, along which prominent clouds such as 20kmC (Arm III) and 50kmC (Arm V) are orbiting, and that the innermost disc structures such as CND and minispirals can be understood as systems of spiral arms organized with a unified rule, as summarized in figure 14.

Theories and simulations to understand the distribution and motion of molecular gas in the GC have been extensively developed over decades, predicting different types of flow models in the CMZ and circum-nuclear regions (Rodriguez-Fernandez & Combes 2008; Wada et al. 2011; Kim & Stone 2012; Krumholz & Kruijssen 2015; Krumholz et al. 2017; Ridley et al. 2017; Sormani et al. 2019 ; Sormani et al. 2020; Tress et al. 2020): The simulations suggest that symmetric spirals of grand design mimicking Arms I and II are generated as a result of galactic shock waves in a bar potential, carrying the gas to the innermost regions and giving rise to CND and mini-spiral-like structures. However, even if such mechanism works, the efficiency of the inward flow must be extremely low, because the mass ratio between the innermost arms and the entire CMZ is very low as shown in table 1. The proposed new view of the innermost spiral structure, including the CND and minispirals (associated with arms VI and VII, respectively), would provide further observational constraints on the model and adds information to a more precise understanding of the CMZ.

Below we discuss some specific topics related to the individual arm structures.

5.2 Comparison with far-infrared dust map

We show in figure 15 a preliminary comparison of the arm structure in the ^{13}CO $(J = 1 - 0)$ line with the image of the CMZ in a dust column density map computed from the Herschel HiGAL survey at 70, 160, 250 350 and 500 μm. The dataset was reprocessed with an algorithm designed to obtain more accurate measurements of cold, dense filamentary structures, densities and temperatures, by improved subtraction of diffuse foreground and background emission. The five Herschel bands were convolved to the resolution of the 500 μm SPIRE image and a process based on the CUPID-findback algorithm was repeatedly applied until consecutive iterations differed by less than 5% in all pixels. (See also Etxaluze et al. (2011)). Taking an estimated value for the dust beta of 1.6, we derived a dust temperature map which, combined with the flux map, yielded the dust column density map. Additional details about the method and checks on its reliability are given in Guzmán et al. (2015).

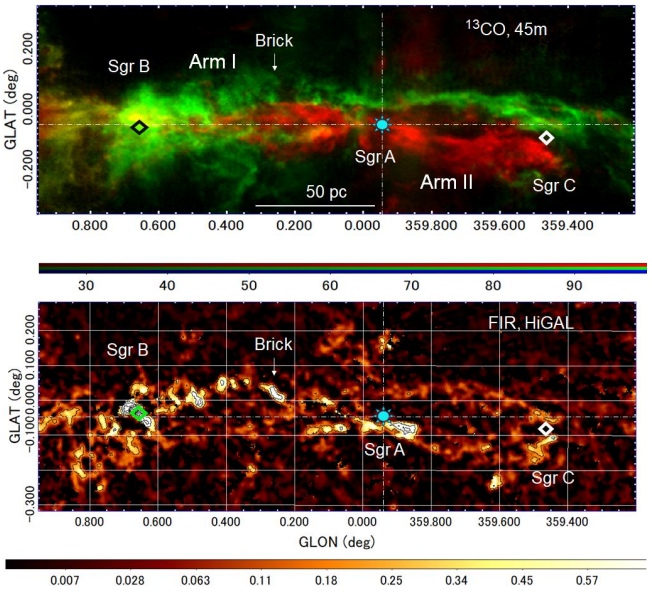

Fig. 15. [Top] Masked moment 0 map in ^{13}CO $(J = 1 - 0)$ Arm I (green) and II (red) (same as the top panel of figure 9) compared with [bottom] a Herschel FIR-derived dust column-density map (Guzmán et al. 2015) (bottom) with the intensity indicated by the bar in units of grams cm^{-2} with contours every 0.7 starting at 0.2. Alt text: Moment 0 map of Arm I+II compared with far-infrared dust map.

It is clear that the warped dust ring coincides closely with the molecular-line ring composed of Arm I and II. The infinity shape suggested in the integrated-intensity maps in molecular lines and dust emission (Molinari et al. 2011) can be traced in the FIR dust map, whereas it does not show up so clearly here in the ^{13}CO $(J = 1 - 0)$ map resolved in the $(l, b, v_{\rm LSR})$ space. Interestingly the dust "Brick" (G+0.25+0.02) (Henshaw et al. 2019; Walker et al. 2021; Ginsburg et al. 2023) is clearly seen in FIR, but is hardly visible in this CO map, which indicates that the cloud is displaced from the molecular arms, or the LV masking function used here was too simple.

Arm III, which is not shown here in ^{13}CO $(J = 1 - 0)$, is visible in the FIR map as a short horizontal belt near Sgr A*.

5.3 20kmC & Arm III; 50kmC & Arm V

The region of the inner arms, $|l| \lesssim 0.^\circ 2$ (~ 30 pc) around Sgr A*, contains many well-known molecular clouds, including 20kmC (Takekawa et al. 2017a) and 50kmC (Tsuboi et al. 2009). In this

subsection we examine the validity of our view that these two clouds are associated with Arms III and V, respectively, in Galactic rotation. In figures 16 and 17 we show the LVDs of Arm III at $b = -0^\circ.072$ and Arm V at $b = -0^\circ.055$ in the $H^{13}CN$ $(J = 1-0)$ line from ACES.

Figure 16 shows that 20kmC is located along the straight LV ridge of Arm III and constitutes the main and densest part of the arm. Careful inspection of the LVD reveals two parallel LV ridges separated by an absorption belt. In the bottom panel we enlarge the brightest region of Arm III (20kmC) by a contour map and an $H^{13}CN$ $(J = 1-0)$ line spectrum.

The line profile (see also subsection 5.4) exhibits a double-horn profile, which may be attributed either to (i) an expanding cylinder (not a shell), (ii) absorption of the background continuum emission, or (iii) self absorption.

The possibility of an expanding cylinder (i) is very unlikely. We may also rule out the possibility of an expanding shell model that postulates an elliptical LV feature. Absorption of background light (ii) is also unlikely because the region is ~ 7 pc away from Sgr A* on the sky. We may therefore conclude that the feature is due to self-absorption of the $H^{13}CN$ $(J = 1-0)$ line. Similar absorption belt is seen in CS $(J = 2-1)$ by ACES and HCN $(J = 4-3)$ by ASTE 10-m observations. However, no absorption feature is seen in the ^{13}CO $(J = 1-0)$ line by the 45-m observations.

The 50kmC is located on the exact extension of Arm V in the LVD as indicated by the dashed line in the top panel of figure 17. The bottom panel enlarges the LVD of 50kmC. The cloud's LV ridge is tilted in the same sense at $dv/dl \sim 3000$ km s^{-1}deg^{-1} as that of Arm V, rotating in the same sense as the overall Galactic rotation. This kinematical alignment suggests its association with Arm V. Since no absorption against the radio continuum of Sgr A is observed, it may be located on the far side of Sgr A.

5.4 Absorption of the Sgr A* continuum emission

We have so far assumed that 20kmC is in front of and 50kmC is beyond Sgr A*. In order to examine if this orientation is plausible, we inspect the line profile of 20kmC and the absorption of the $H^{13}CN$ $(J = 1-0)$ line against radio continuum from Sgr A* in figure 18. The 20kmC shows a clear double-peaked emission profile indicative of self absorption. In the bottom panel we show the spectrum toward Sgr A*, which exhibits various absorption lines due to molecular clouds on the near side to the Sun. The 20kmC cloud appears as the absorption feature around $v_{\rm LSR} \sim 20$ km s^{-1}, partially overlapping the local and disc absorption lines. This fact indicates that 20kmC is on the near side of Sgr A*, consistent with the orientation proposed in figure 14.

On the other hand, 50kmC shows up neither in emission nor absorption, probably due to absence of associated gas in this direction. Therefore, its line-of-sight location cannot be argued from this figure.

5.5 Circum-nuclear non-circular flow

The top panel of figure 19 shows an LVD in CS $(J = 2-1)$ averaged between $b = -0^\circ.1$ and 0°, revealing high-velocity non-circular flows. As a whole, the LVD mimics that of the CMZ in a wider field of the inner Galaxy, exhibiting a tilted ellipse composed of curved spurs and stripes. We call this structure the "mini-CMZ" in LVD.

The second panel shows a close up of the circum-nuclear region in a narrow range of latitude at $b = -0^\circ.02$ averaged in ± 50 chan-

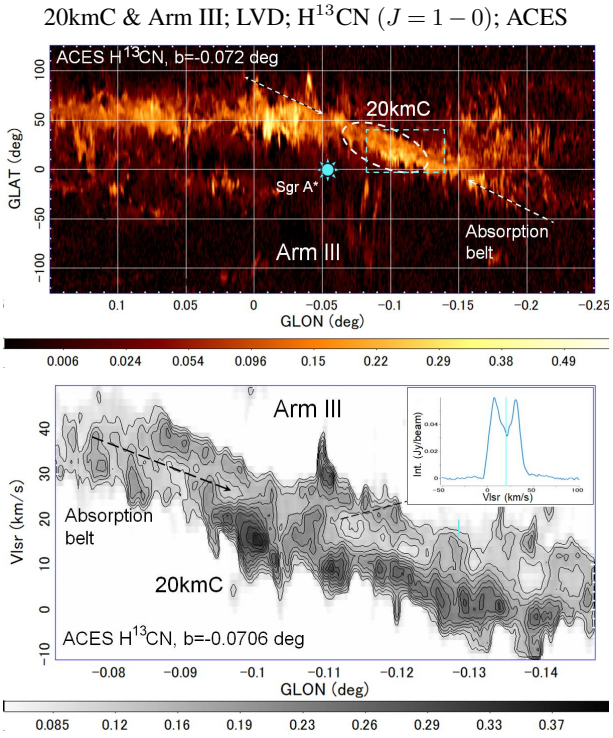

Fig. 16. [Top] 20kmC and Arm III in $H^{13}CN$ $(J = 1-0)$ at $b = -0^\circ.072$ by ACES. [Bottom] Enlargement of Arm III (blue box in top panel), showing an absorption belt. Contours: every 0.025 Jy beam^{-1} starting at 0.1. Insertion displays the line profile where the arrow points. Alt text: LVD of Arm III with 20kmC, and the same but enlarged.

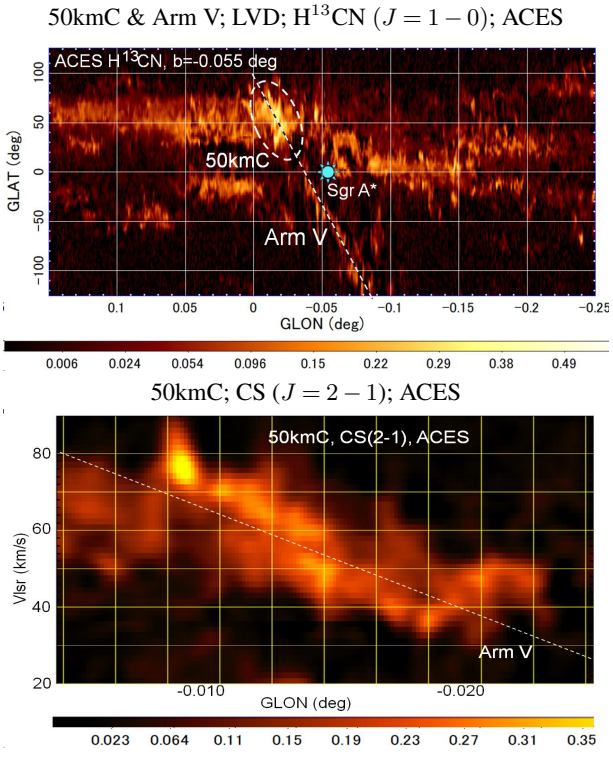

Fig. 17. [Top] LVD of Arm V and 50kmC in $H^{13}CN$ $(J = 1-0)$ at $b = -0^\circ.055$ by ACES, showing 50kmC located on the straight extension of Arm V. [Bottom] LVD across 50kmC at $b = -0^\circ.0462$, showing velocity gradient $dv/dl \sim 3000$ km s^{-1}deg^{-1}, about the same as Arm V. Alt text: LVD of Arm V with 50kmC, and close up of LVD of 50kmC.

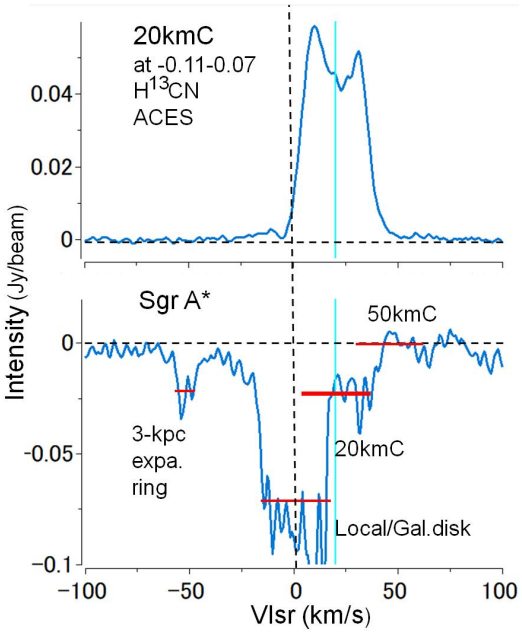

Fig. 18. [Top] The $H^{13}CN$ $(J = 1 - 0)$line profile of the 20kmC at $(l, b) = (-0^\circ.11, -0^\circ.07)$, showing self absorption. [Bottom] Absorption line profile of the same line toward Sgr A*. The 20kmC absorbs the continuum from Sgr A* as marked by the horizontal red line, indicating that it is located on the near side. 50kmC does not show any emission or absorption. The local/disc gas on the near-side as well as the 3-kpc expanding ring appear as the absorption lines. Alt text: $H^{13}CN$ $(J = 1 - 0)$-line profile of 20kmC, and absoprtion profile of Sgr A*.

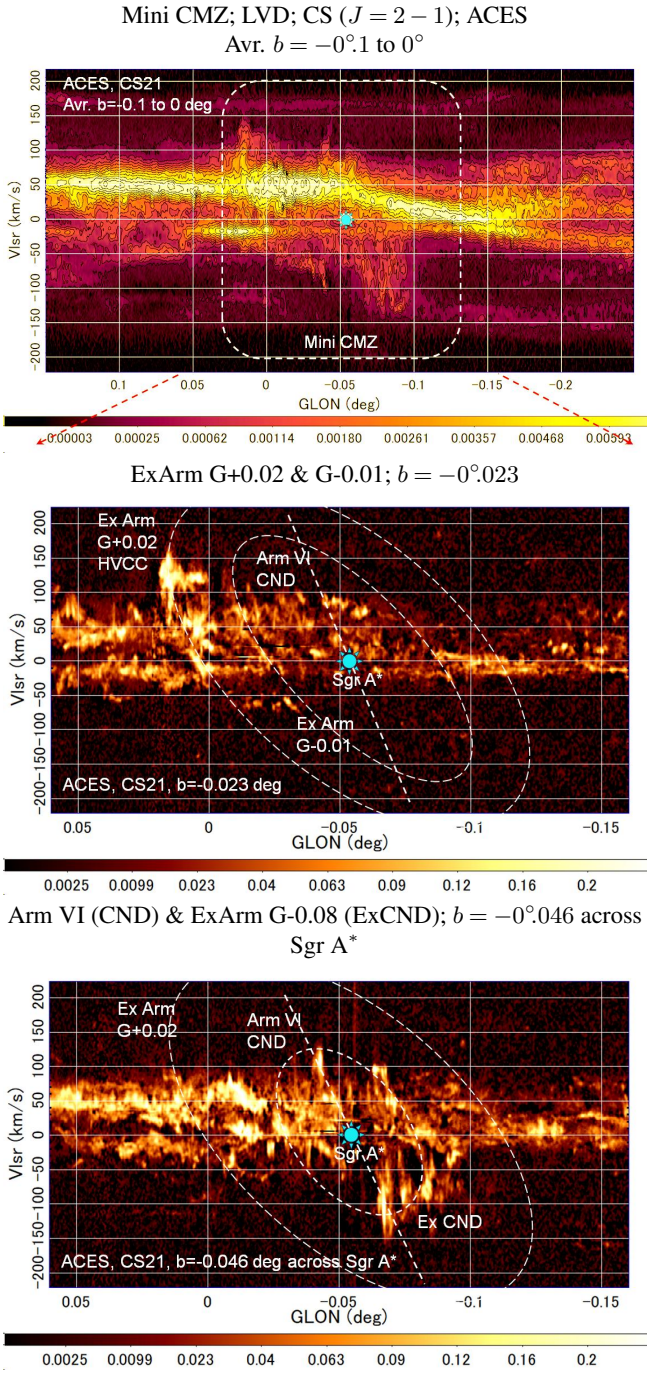

Fig. 19. [Top] CS $(J = 2 - 1)$ LVD by ACES averaged from $b = -0^\circ.1$ to 0°, revealing the "mini CMZ". [Middle] Close up of the mini CMZ at $b = -0^\circ.02$ (mean in ± 50 channels). An expanding arm/ring feature at G+0.02-0.02 is found crossing the HVCC, approximately fitted by an ellipse as indicated by the tilted dashed ellipse "ExArm G+0.02". An inner expanding feature newly found here is marked by the dashed ellipse marked "ExArm G−0.01". [Bottom] LVD channel across Sgr A*. The non-circular flow component associated with the CND is marked by the inner red ellipse "ExCND". Alt text: LVDs of innermost region of CMZ by ACES, showing high-velocity expansion and non-circular motions.

nels ($\pm 25''$), showing the curved spurs more clearly. The bright and curved LV ridge can be fitted by a tilted ellipse centered on Sgr A*, as indicated by the dashed line with expanding velocity as high as $V_{\rm ex} \sim 200$ km s^{-1}rotating at $V_{\rm rot} \sim 120$ km s^{-1}. The brightest part coincides in position and velocity with the HVCC G+0.02-0.02 ($v_{\rm LSR} \sim 100$ km s^{-1}). We call this elliptical feature the "ExArm G+0.02" after the longitude of its brightest edge.

There is another elliptical spur marked by the inner dashed ellipse with suggested expanding velocity of $V_{\rm ex} \sim 150$ km s^{-1}and rotation velocity $V_{\rm rot} \sim 130$ km s^{-1}, which we name "ExArm G-0.01".

However, both ExArms are highly lopsided with respect to Sgr A*, and no counterparts are seen at any latitudes in the present range ($b = -0^\circ.1$ to 0°). Such a lopsided property is also similar to the CMZ.

The 3rd panel shows the same, but at $b = -0^\circ.046$ across Sgr A*, showing the complex associated with the CND (Wright et al. 2001; Montero-Castaño et al. 2009; Martín et al. 2012; Tsuboi et al. 2018; Hsieh et al. 2021). A remarkable half-ellipse feature is associated, starting from the negative-velocity end of Arm VI (CND). The entire feature can be fitted by an ellipse as indicated by the dashed line with $V_{\rm ex} \sim 100$ km s^{-1} and $V_{\rm rot} \sim 100$ km s^{-1}. We call this ellipse the "ExCND (ExArm G-0.08)" after its eastern-edge longitude. Note that this feature is also lopsided.

5.6 Faint 200-pc EMR

Besides the main structures of the CMZ like the GC Arms, figures 1 to 7 also exhibit various features surrounding these. One of such features is the expanding molecular ring (EMR) commonly ap-

pearing in these LVDs, which are marked in figure 7 by the nearly horizontal dashed lines EMR+ and EMR-. It has long been debated whether the EMR is due to an expanding ring caused by an explosion at the center (Kaifu et al. 1972 ; Scoville 1972 ; Sofue 2017), or a "parallelogram" due to non-circular gas flow in a bar potential(Binney et al. 1991; Sormani et al. 2015; Sormani et al. 2018 ; Sormani et al. 2019 ; Sormani et al. 2020; Tress et al. 2020) (see Henshaw et al. (2023) for a review).

A discussion of these features is beyond the scope of this paper, but we point out that the EMR is fainter than the main Arms I and II by a factor of $\sim 10^{-2}$ in surface brightness of the molecular lines, and the total mass is an order of magnitude smaller than that of the CMZ (Sofue 2017). Furthermore, the EMR has a large vertical extension above and below the CMZ over $\sim \pm 100$ pc, which deviates significantly from the thickness-radius relationship in figure 13. Therefore, in order for the EMR (parallelogram) to act as a mass supplier to the CMZ, the gas transported from the outer Galactic disc with a thickness of $\sim$ 20–30 pc must first be lifted to that height and then quickly compressed to the CMZ of thickness $\sim$ 10–20 pc. In this context, it has been recently argued that the western wing of the EMR may be a high-velocity ($\sim \pm$100–200 km s^{-1}) and high-altitude ($z/2 \sim$ 20–60 pc) molecular inflow with a length of $\sim$ 200 pc, acting to transport the gas into the CMZ (Veena et al. 2024).

6 Summary

Analyzing the molecular-line cubes of the Galactic Centre taken with the ALMA (CS ($J = 2-1$) and H^{13}CN ($J = 1-0$)), Nobeyama 45-m telescope (^{13}CO ($J = 1-0$)), and ASTE 10-m telescope (H^{13}CN ($J = 1-0$)), we studied the kinematic behavior of GC Arms I to VI identified in the longitude-velocity diagrams (LVDs). The galactocentric radii of the Arms are determined by the dv/dl method assuming a flat rotation curve. Applying the LV-masking method, we also obtained moment 0 maps integrated in the velocity range within $\pm \sim$ 7.5–10 km s^{-1}from the LV ridges of the Arms. We find that the radius of the Nth arm is approximately given by $R \sim 630 \times 0.40^N$ pc, suggesting a logarithmic spiral or Bode's law-like discreteness of the orbits. If we consider the minispirals to constitute Arm VII, the relation holds from $N = 1$ (I) to 7 (VII). The vertical full thickness of the arms is approximated by $z \sim 0.7(R/1\ \mathrm{pc})^{0.7}$ pc.

Unifying the derived parameters of the arms and rings, we summarize the results in figure 14 as a schematic view of the warping CMZ: Arms I and II share most of the mass (volume) of CMZ; the inner arms share a few percent of the CMZ mass (volume); hence the accretion is slow; the disc thickness decreases toward the centre; and the warping amplitude or the arm's tilt from the galactic plane increases toward the centre.

Acknowledgments

This paper makes use of the following ALMA data: ADS/JAO.ALMA#2021.1.00172.

ALMA is a partnership of ESO (representing its member states), NSF (USA) and NINS (Japan), together with NRC (Canada), NSTC and ASIAA (Taiwan), and KASI (Republic of Korea), in cooperation with the Republic of Chile.

The Joint ALMA Observatory is operated by ESO, AUI/NRAO and NAOJ.

The data analysis in this paper was partially performed at the Astronomical Data Center of the National Astronomical Observatories of Japan.

C. Battersby gratefully acknowledges funding from National Science Foundation under Award Nos. 2108938, 2206510, and CAREER 2145689, as well as from the National Aeronautics and Space Administration through the Astrophysics Data Analysis Program under Award "3-D MC: Mapping Circumnuclear Molecular Clouds from X-ray to Radio," Grant No. 80NSSC22K1125.

COOL Research DAO is a Decentralised Autonomous Organisation supporting research in astrophysics aimed at uncovering our cosmic origins.

J.M.D.K. gratefully acknowledges funding from the European Research Council (ERC) under the European Union's Horizon 2020 research and innovation programme via the ERC Starting Grant MUSTANG (grant agreement number 714907).

KMD acknowledges support from the European Research Council (ERC) Advanced Grant MOPPEX 833460.vii.

L.C., V.M.R. and I.J.-S. acknowledge support from the grant PID2022-136814NB-I00 by the Spanish Ministry of Science, Innovation and Universities/State Agency of Research MICIU/AEI/10.13039/501100011033 and by ERDF, UE.

V.M.R. also acknowledges support from the grant RYC2020-029387-I funded by MICIU/AEI/10.13039/501100011033 and by "ESF, Investing in your future", from the Consejo Superior de Investigaciones Científicas (CSIC) and the Centro de Astrobiología (CAB) through the project 20225AT015 (Proyectos intramurales especiales del CSIC); and from the grant CNS2023-144464 funded by MICIU/AEI/10.13039/501100011033 and by "European Union NextGenerationEU/PRTR".

I.J.-S. acknowledges support from ERC grant OPENS, GA No. 101125858, funded by the European Union. Views and opinions expressed are however those of the author(s) only and do not necessarily reflect those of the European Union or the European Research Council Executive Agency. Neither the European Union nor the granting authority can be held responsible for them.

P. García is sponsored by the Chinese Academy of Sciences (CAS), through a grant to the CAS South America Center for Astronomy (CASSACA).

R.S.K. thanks the 2024/25 Class of Radcliffe Fellows for highly interesting and stimulating discussions, financial support from the European Research Council via ERC Synergy Grant "ECOGAL" (project ID 855130), the German Excellence Strategy via (EXC 2181 - 390900948) "STRUCTURES", the German Ministry for Economic Affairs and Climate Action in project "MAINN" (funding ID 50OO2206), Ministry of Science, Research and the Arts of the State of Baden-Württemberg through bwHPC and the German Science Foundation through grants INST 35/1134-1 FUGG and 35/1597-1 FUGG, and also for data storage at SDS@hd funded through grants INST 35/1314-1 FUGG and INST 35/1503-1 FUGG.

D. Riquelme-Vásquez acknowledges the financial support of DIDULS/ULS, through the project PAAI 2023.

Data availability

The single-dish data underlying this article are available at https://www.nro.nao.ac.jp/ ∼nro45mrt/html/ results/data.html. The interferometer data were taken from the internal release version of the 12m+7m+TP (Total Power)-mode data from the ALMA cycle 8 Large Program "ALMA Central Molecular Zone Exploration Survey" (ACES, 2021.1.00172.L).

Conflict of interest

The authors declare that there is no conflict of interest.

References

Bally, J., Stark, A. A., Wilson, R. W., et al. 1987, ApJS, 65, 13. doi:10.1086/191217

Bally, J., Stark, A. A., Wilson, R. W., et al. 1988, ApJ, 324, 223. doi:10.1086/165891

Binney J., Gerhard O. E., Stark A. A., Bally J., Uchida K. I., 1991, MNRAS, 252, 210

Etxaluze, M., Smith, H. A., Tolls, V., et al. 2011, AJ, 142, 134. doi:10.1088/0004-6256/142/4/134

Ginsburg, A., Bally, J., Barnes, A. T., et al. 2024, ApJL, 968, L11. doi:10.3847/2041-8213/ad47fa

Ginsburg, A., Barnes, A. T., Battersby, C. D., et al. 2023, ApJ, 959, 36. doi:10.3847/1538-4357/acfc34

Ginsburg, A., Henkel, C., Ao, Y., et al. 2016, AA, 586, A50. doi:10.1051/0004-6361/201526100

Gravity Collaboration, Abuter, R., Amorim, A., et al. 2019, AA, 625, L10. doi:10.1051/0004-6361/201935656

Guzmán, A. E., Sanhueza, P., Contreras, Y., et al. 2015, ApJ, 815, 130. doi:10.1088/0004-637X/815/2/130

Henshaw, J. D., Barnes, A. T., Battersby, C., et al. 2023, Protostars and Planets VII, 534, 83. doi:10.48550/arXiv.2203.11223

Henshaw, J. D., Ginsburg, A., Haworth, T. J., et al. 2019, MNRAS, 485, 2457. doi:10.1093/mnras/stz471

Henshaw, J. D., Krumholz, M. R., Butterfield, N. O., et al. 2022, MNRAS, 509, 4758. doi:10.1093/mnras/stab3039

Henshaw, J. D., Longmore, S. N., Kruijssen, J. M. D., et al. 2016, MNRAS, 457, 2675.

Heywood, I., Rammala, I., Camilo, F., et al. 2022, ApJ, 925, 165. doi:10.3847/1538-4357/ac449a

Hsieh, P.-Y., Koch, P. M., Kim, W.-T., et al. 2021, ApJ, 913, 94. doi:10.3847/1538-4357/abf4cd

Iwata, Y., Oka, T., Takekawa, S., et al. 2023, ApJ, 950, 25. doi:10.3847/1538-4357/acc9b0

Kaifu, N., Kato, T., & Iguchi, T. 1972, Nature Physical Science, 238, 105

Kim, W.-T. & Stone, J. M. 2012, ApJ, 751, 124. doi:10.1088/0004-637X/751/2/124

Kruijssen, J. M. D., Dale, J. E., & Longmore, S. N. 2015, MNRAS, 447, 1059. doi:10.1093/mnras/stu2526

Kruijssen, J. M. D., Dale, J. E., Longmore, S. N., et al. 2019, MNRAS, 484, 5734. doi:10.1093/mnras/stz381

Krumholz, M. R. & Kruijssen, J. M. D. 2015, MNRAS, 453, 739. doi:10.1093/mnras/stv1670

Krumholz, M. R., Kruijssen, J. M. D., & Crocker, R. M. 2017, MNRAS, 466, 1213. doi:10.1093/mnras/stw3195

Martín, S., Martín-Pintado, J., Montero-Castaño, M., et al. 2012, AA, 539, A29. doi:10.1051/0004-6361/201117268

Molinari, S., Bally, J., Noriega-Crespo, A., et al. 2011, ApJL, 735, L33. doi:10.1088/2041-8205/735/2/L33

Montero-Castaño, M., Herrnstein, R. M., & Ho, P. T. P. 2009, ApJ, 695, 1477. doi:10.1088/0004-637X/695/2/1477

Morris, M. & Serabyn, E. 1996, ARA&A, 34, 645. doi:10.1146/annurev.astro.34.1.645

Nogueras-Lara, F. 2022, AA, 668, L8. doi:10.1051/0004-6361/202244934

Oka, Tomoharu, Hasegawa, T., Sato, F., et al. 1998, ApJS, 118, 455. doi:10.1086/313138

Oka, T., Nagai, M., Kamegai, K., et al. 2011, ApJ, 732, 120. doi:10.1088/0004-637X/732/2/120

Oka, T., Uruno, A., Enokiya, R., et al. 2022, ApJS, 261, 13. doi:10.3847/1538-4365/ac6bfc

Oka, T., White, G. J., Hasegawa, T., et al. 1999, ApJ, 515, 249. doi:10.1086/307029

Ridley, M. G. L., Sormani, M. C., Tre, R. G., et al. 2017, MNRAS, 469, 2251. doi:10.1093/mnras/stx944

Rodriguez-Fernandez, N. J. & Combes, F. 2008, AA, 489, 115. doi:10.1051/0004-6361:200809644

Sánchez-Monge, Á., Schilke, P., Ginsburg, A., et al. 2018, AA, 609, A101. doi:10.1051/0004-6361/201730425

Sawada, T., Hasegawa, T., Handa, T., et al. 2004, MNRAS, 349, 1167.

Scoville, N. Z. 1972, ApJL, 175, L127

Shibata, K. & Uchida, Y. 1986, PASJ, 38, 631

Shirley, Y. L. 2015, PASP, 127, 299. doi:10.1086/680342

Sofue, Y. 1993, PASP, 105, 308. doi:10.1086/133148

Sofue, Y. 1995, PASJ, 47, 527.

Sofue, Y. 2006, PASJ, 58, 335. doi:10.1093/pasj/58.2.335

Sofue, Y. 2013, PASJ, 65, 118. doi:10.1093/pasj/65.6.118

Sofue, Y. 2017, MNRAS, 470, 1982

Sofue, Y. 2020, MNRAS, 498, 1335. doi:10.1093/mnras/staa2389

Sofue, Y. 2022, MNRAS, 516, 907. doi:10.1093/mnras/stac2243

Sofue, Y. 2024, MNRAS, 532, 4187. doi:10.1093/mnras/stae1724

Sormani, M. C., Binney, J., & Magorrian, J. 2015, MNRAS, 454, 1818.

Sormani, M. C., Tress, R. G., Ridley, M., et al. 2018, MNRAS, 475, 2383. Bar plg doi:10.1093/mnras/stx3258

Sormani, M. C., Tress, R. G., Glover, S. C. O., et al. 2019, MNRAS, 488, 4663.

Sormani, M. C., Tress, R. G., Glover, S. C. O., et al. 2020, MNRAS, 497, 5024. doi:10.1093/mnras/staa1999

Takekawa, S., Oka, T., Iwata, Y., et al. 2017b, ApJL, 843, L11. doi:10.3847/2041-8213/aa79ee

Takekawa, S., Oka, T., & Tanaka, K. 2017a, ApJL, 834, 121. doi:10.3847/1538-4357/834/2/121

Tanaka, K., Nagai, M., Kamegai, K., et al. 2018, ApJS, 236, 40. doi:10.3847/1538-4365/aab9a5

Tokuyama, S., Oka, T., Takekawa, S., et al. 2019, PASJ, 71, S19. doi:10.1093/pasj/psy150

Tress, R. G., Sormani, M. C., Glover, S. C. O., et al. 2020, MNRAS, 499, 4455. doi:10.1093/mnras/staa3120

Tsuboi, M., Handa, T., & Ukita, N. 1999, ApJS, 120, 1. doi:10.1086/313165

Tsuboi, M., Kitamura, Y., Uehara, K., et al. 2017, ApJ, 842, 94. doi:10.3847/1538-4357/aa74e3

Tsuboi, M., Kitamura, Y., Uehara, K., et al. 2018, PASJ, 70, 85. doi:10.1093/pasj/psy080

Tsuboi, M., Miyazaki, A., & Okumura, S. K. 2009, PASJ, 61, 29. doi:10.1093/pasj/61.1.29

Uehara, K., Tsuboi, M., Kitamura, Y., et al. 2019, ApJ, 872, 121. doi:10.3847/1538-4357/aafee7

Veena, V. S., Kim, W.-J., Sánchez-Monge, Á., et al. 2024, AA, 689, A121. doi:10.1051/0004-6361/202450902

Wada, K., Baba, J., & Saitoh, T. R. 2011, ApJ, 735, 1. doi:10.1088/0004-637X/735/1/1

Walker, D. L., Longmore, S. N., Bally, J., et al. 2021, MNRAS, 503, 77. doi:10.1093/mnras/stab415

Wright, M. C. H., Coil, A. L., McGary, R. S., et al. 2001, ApJ, 551, 254. doi:10.1086/320089

Yan, Q.-Z., Walsh, A. J., Dawson, J. R., et al. 2017, MNRAS, 471, 2523. doi:10.1093/mnras/stx1724

Zhao, J.-H., Morris, M. R., Goss, W. M., et al. 2009, ApJ, 699, 186. doi:10.1088/0004-637X/699/1/186

Appendix 1 IMSHIFT-relieving method

In order to abstract tilted LV stripes representing rotating arms in the CMZ using single dish observations, we apply the IMSHIFT relieving technique, which is a modification of the "background-filtering" (BGF) (pressing) method (Sofue 1993). This method subtracts extended components with scale sizes greater than a threshold value (here 5 pixels) in one direction (here in galactic longitude), so that it enhances oblique and vertical LV stripes. This

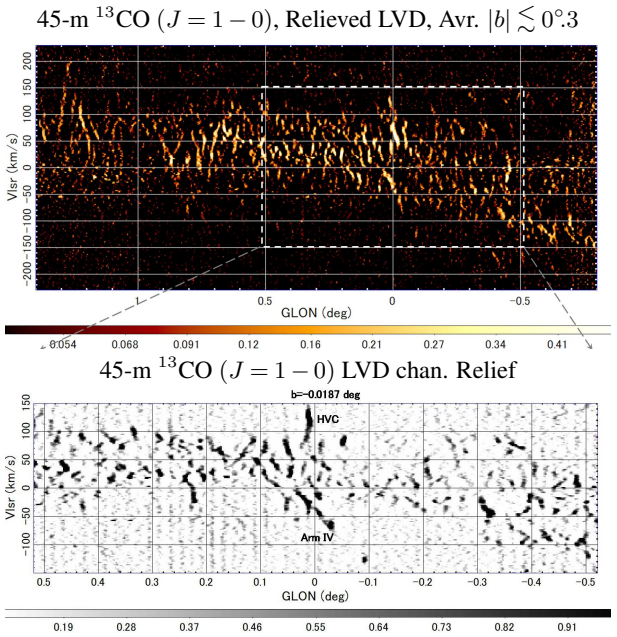

Fig. 20. ^{13}CO $(J=1-0)$ IMSHIFT-relieved LVDs (longitude-velocity diagrams) in the CMZ in ^{13}CO $(J=1-0)$ line observed with the 45-m telescope in the whole area (top) and the central region at $b=-0^\circ.02$ (bottom). Alt text: 2 LVDs by applying the IMSHIFT-relieving method.

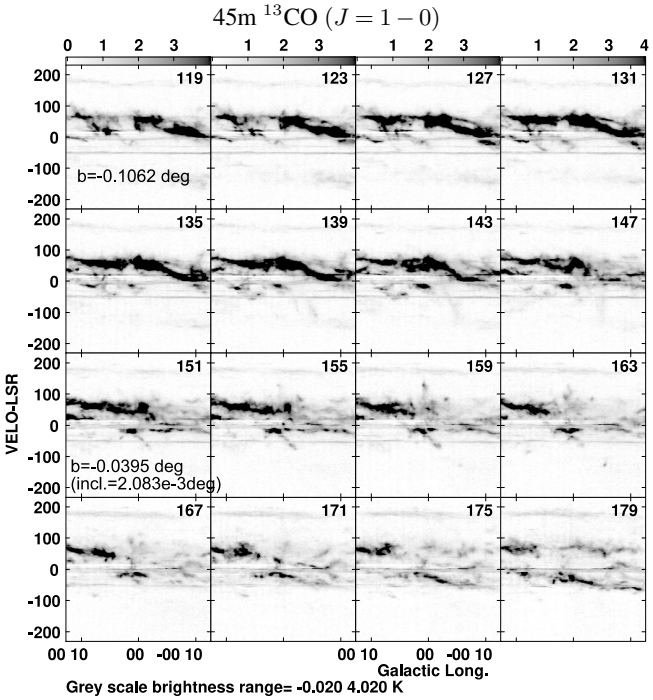

Fig. 21. 45-m latitudinal channel LVDs (longitude-velocity diagrams) in the ^{13}CO $(J=1-0)$ line from $b=-0^\circ.06$ (119-th channel) to $+0^\circ.21$ (179-th) every $0^\circ.0083$ of the central $\pm 0^\circ.2$ about $l=0^\circ$. Alt text: Latitudinal channel LVDs in ^{13}CO $(J=1-0)$from 45-m telescope.

method, therefore, suppresses the horizontal LV stripes (contamination) due to the fore- and background Galactic disc. We confirmed that there are no significant differences in the results when the relieving size is from $\delta x \sim 3$ to 10 pix. Figure 20 shows an example of relieved LVD averaged in $|b| \lesssim 0^\circ.3$ in the whole CMZ in ^{13}CO $(J=1-0)$ line, and the bottom panel is enlargement in the central region at a fixed latitude.

The method consists of the following procedure. Let the original map represents intensity distribution $T(x,y)$. The relieved intensity is defined by

$$\Delta T(x,y) = (\Delta T^+ + \Delta T^-)/2 \qquad \text{(A1)}$$

where $\Delta T^+ = T(x,y) - T(x+\delta x, y)$ and $\Delta T^- = T(x,y) - T(x-\delta x, y)$. We then replace the pixel values to zero, if $\Delta T < 0$. In the present analysis, we adopt a relieving size of $\delta x = 5$pix $\sim 37''.5 = 1.5$ pc in the longitude direction. However, the following point may be kept in mind when using it: The method suppresses structures wider than the threshold width, the obtained LVDs are not useful to discuss large-scale arms and rings, particularly in the outer CMZ.

Appendix 2 Channel LVDs

We present latitudinal channel maps of LVDs of the central $l \sim \pm 0^\circ.2$ region in ^{13}CO $(J=1-0)$ line from 45-m telescope in figure 21, same but IMSHIFT relieved in figure 22 , and in H^{13}CN $(J=1-0)$ line from ASTE 10-m in figure 23. Figures 24 shows CS $(J=2-1)$ and H^{13}CN $(J=1-0)$-line channel LVDs from ACES of the central $\sim \pm 0^\circ.1$ region. These figures along with the original cubes were used to find and identify an arm as a straight LV ridge extending over ~ 100 km s^{-1}, and to confirm that the arm is not artifact specific to a certain channel, but is a real object by comparing the feature with those continuously appearing in the neighboring multiple channels.

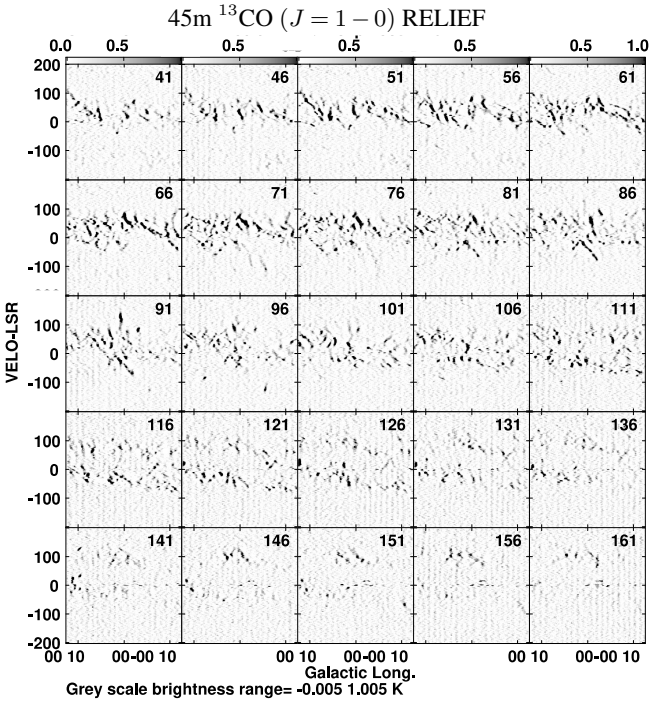

Fig. 22. 45-m IMSHI-relief LVDs in ^{13}CO $(J=1-0)$ from $b=-0^\circ.125$ (41-th channel) to $+0^\circ.125$ (161-th) every $0^\circ.0105$. Alt text: Latitudinal channel LVDs (relieved) in ^{13}CO $(J=1-0)$from 45-m telescope.

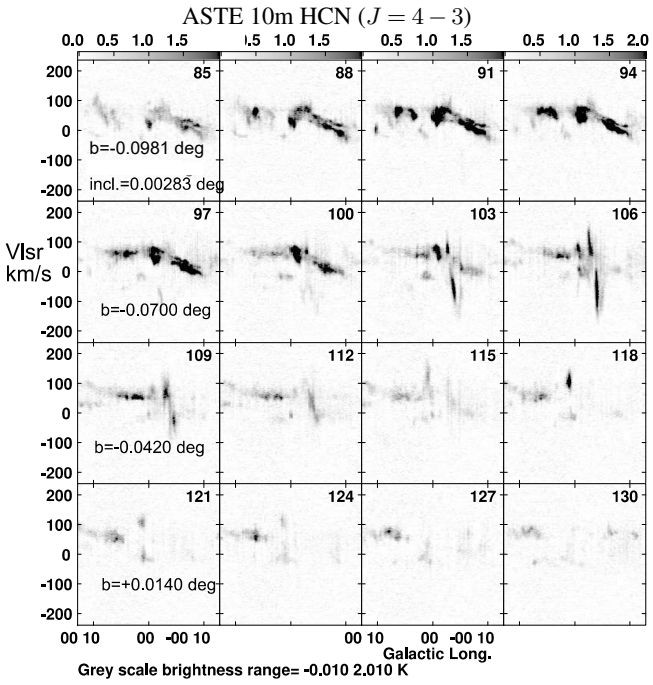

Fig. 23. Channel LVDs in HCN ($J = 4 - 3$) by ASTE 10-m telescope. Alt text: Latitudinal channel LVDs in HCN ($J = 4 - 3$) form ASTE-10 m.

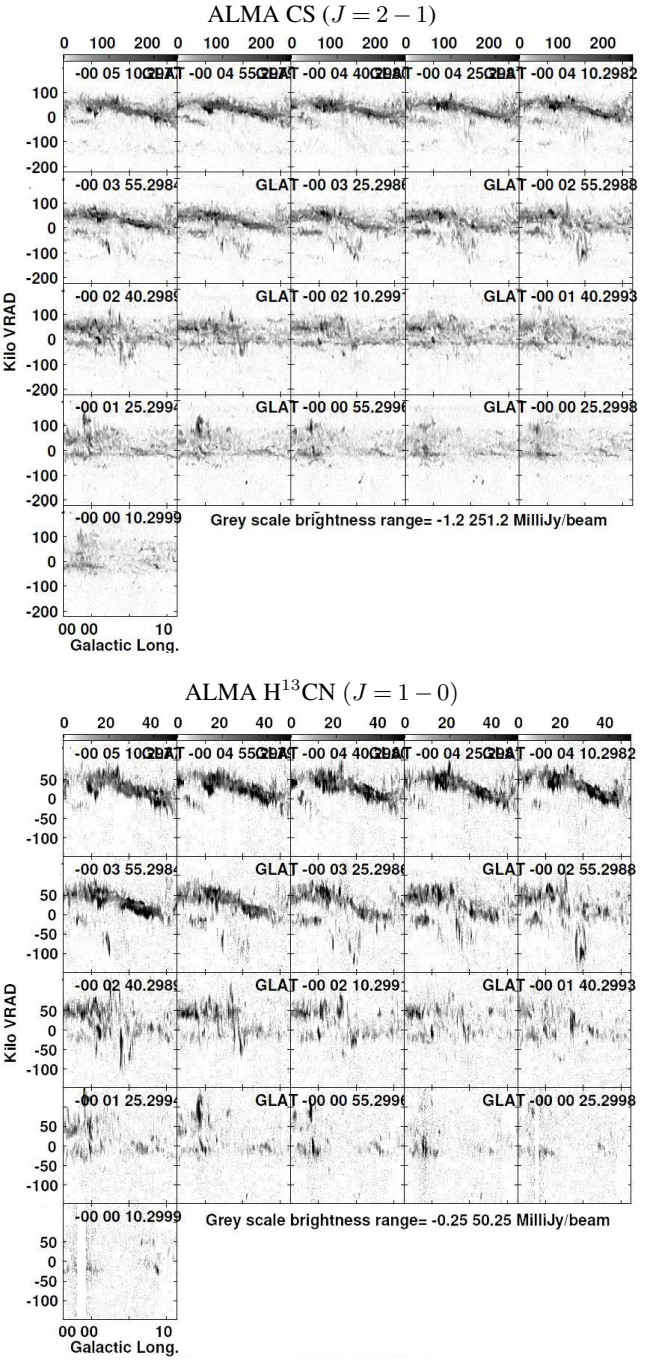

Fig. 24. ACES latitude-channel maps of LVDs in CS ($J = 2 - 1$) (top) and $H^{13}CN$ ($J = 1 - 0$) (bottom) of the central $\pm 0^{\circ}.12$ about Sgr A*. Alt text: Latitudinal channel LVDs in CS ($J = 2 - 1$) and $H^{13}CN$ ($J = 1 - 0$) by ACES.